



TECHNISCHE
UNIVERSITÄT
WIEN
Vienna University of Technology

DIPLOMARBEIT

Large-scale control of nitrogen-vacancy quantum bit arrays in diamond

ausgeführt am Atominstitut der Technischen Universität Wien
unter der Anleitung von

Univ. Prof. Dr. Hannes-Jörg Schmiedmayer
Projektass. Dr. Michael Trupke
Projektass. Dipl.-Ing. Andreas Angerer

eingereicht an der
Technischen Universität Wien
Fakultät für Physik

von

Johannes Leitner
Matrikelnummer 1025152
Schönbrunner Straße 260/2/22, 1120 Wien

Wien, am 13. Dezember 2016

Abstract

During the last ten years, basic quantum operations on a single electronic spin in the nitrogen-vacancy centre (NV) in diamond have been a rich field of study. These defects have become promising candidates as robust, long-lived qubits. However, in order to realize quantum computers with the help of these qubits one has to find a way to create and control a system of many qubits. One promising way will be introduced in this thesis.

Using a wire grid, which is directly produced on the diamond sample, in combination with a STIRAP-inspired (stimulated Raman adiabatic passage) transition gives access to manipulate a specific NV within a large number of other NVs. The reason is that STIRAP requires two photons in order to perform the transfer, which is utilized with the wire grid. By sending one microwave pulse through a horizontal wire and the second pulse through a vertical wire, the condition for STIRAP is only fulfilled at the junction of both. Furthermore, introducing a detuning of these pulses is not only necessary to truly perform a STIRAP-inspired (two-tone) transition but also reduces the effects of the microwave signals at other crossings.

The first part of this thesis describes the basic physics of the NV and discusses STIRAP. After explaining the experimental setup the implementation of the two-tone pulses is demonstrated.

The second part is dedicated to the usage of the wire grid. First, the performance of the wire grid is anticipated by using a single wire with a single NV, as single wire measurements are easier to control and better understood. The dependence on the microwave power of the two-tone efficiency is obtained and a comparison to the dependence on the distance is made. Additionally, the time-behaviour of the two-tone transfer is observed depending on the detuning of the two-tone pulses. After getting a good estimate of the performance of the wire grid the grid itself is implemented in the experimental setup. Measurements confirm the expected performance and the possibility to address a single site without affecting any other sites. Finally, a way to cancel out any unintended effects at neighbouring crossings is demonstrated in order to show that the wire grid can be built smaller while maintaining high performance qubit control.

Acknowledgements

It has been a great pleasure to work on my thesis at the Atominstitut, not only for the interesting science but also for the people who I got to know during this time. The whole group supported me in my experiment with fruitful discussions and with a helping hand in difficult times. Some people, however, influenced me more as I was working closely together with them.

I would like to thank especially Dipl.-Ing. Andreas Angerer, who not only introduced me to NV⁻ science at the start of my thesis, but always had an open ear for my problems and struggles. His enthusiasm for science has affected me since day one and his drive to make things happen spurred me on to do the same. Without his help and knowledge about NV⁻s, the experiment and the software this thesis would not have been possible. In particular, he helped me to move the experiment to another room, rebuild it and understand the experimental setup. Furthermore, he introduced me to the computer language Python and showed me how to implement a measurement scheme using the measuring software. During my time working on the experiment he helped me many times with all kinds of problems.

Moreover, I want to thank my supervisor Dr. Michael Trupke, with whom I had the pleasure to work with before. He welcomed me with open arms and guided me throughout my thesis. His expertise in the field of NV⁻ science and his extraordinary ideas helped me many times. It was his idea to address NVs with the help of a wire grid system and designed the basic layout of the grid. Furthermore, he simulated the performance of the wire grid in order to choose the best parameters for the two-tone pulses and to validate the observed data. Additionally, he always had suggestions on how to solve problems and was the mind behind the whole project.

I also want to thank my colleague Daniel Wirtitsch, who joined me the last half year of my work, for helping me with the two-tone transfer measurements and providing a new perspective. We have not only shared the struggle of hours of measuring time but also the joy of success.

I want to thank Matthias Stüwe for performing the fabrication of the wire grid and the electronics workshop team of the Atominstitut for making the circuit board.

Lastly, I want to thank Dr. Jörg Schmiedmayer, the head of the group, for giving young scientists the possibility to dive into physics and start their career in a cheerful and motivated group.

All in all I can say that choosing the Atominstitut for my thesis was a really good decision and spurred me on to do my best work so far. I learned a lot not only about science but also about programming and how to solve difficult problems with the help of others. My knowledge about quantum, atomic and solid state physics, about optics and microwave usage was greatly expanded and I enjoyed working on the experiment with such fascinating people. Thank you!

Contents

Abstract	i
Acknowledgements	iii
1 Introduction	1
1.1 Overview of the research area	1
1.2 Scalable qubit control	6
2 Basic physics of the NV centre	9
2.1 Structure of the NV centre	9
2.2 Term scheme and optical transitions	9
2.2.1 Optical transitions	11
2.2.2 Spin polarization and fluorescence time traces	12
2.3 Fine- and hyperfine structure	14
2.4 Dephasing and decoherence	16
2.5 Quantum theory of a two-level system	17
2.6 Two-tone control of NV ground state	20
3 Experimental setup	25
3.1 Optical setup	25
3.2 Microwave setup	26
4 Measurement schemes	29
4.1 Optically detected magnetic resonance	29
4.2 Pulsed measurements	29
4.2.1 Rabi nutations	30
4.2.2 Free induction decay measurement	32
4.2.3 Spin echo measurement	35
4.2.4 Two-tone transitions	35
5 Matrix control of qubits	39
5.1 Design and production of chip	40
5.2 Single NV	42
5.3 Chip	48
6 Conclusion and Outlook	61
Bibliography	65
List of figures	68

1 Introduction

1.1 Overview of the research area

Quantum computing has attracted much attention over the last 15 to 20 years and is fuelled by the promise of applications and by rapid experimental progress. However, it became clear from the beginning that the restrictions on the physical system of choice are severe. Fortunately, there are many ways to try and realize quantum computers based on many different physical systems [1]. Some of the most promising systems are trapped ions [2–4], ultracold neutral atoms [5, 6], Rydberg atoms [7], superconducting charge-, flux- and phase-qubits [8], linear optics [9], quantum dots [10] and nitrogen-vacancy centre in diamond [11]. All these systems have their own advantages in quantum information processing. Although there are systems which appear to be better suited for quantum computing at the moment, no physical implementation seems to have a clear edge over the others.

Trapped, laser-cooled atomic ions [2] provide a relatively 'clean' system, because they can be trapped for long times while only experiencing small perturbations from the environment and can be coherently manipulated. The traps normally consist of a certain arrangement of electric and/or magnetic fields (e.g. Paul trap), with which the ions can be stored nearly indefinitely and be localized in space within a few nanometers. By cooling the ions in such a Paul trap with a laser, they form a linear string. The ions in this string are separated in space and the distance is determined by a balance between the confining fields and the mutual Coulomb repulsion (see Fig. 1.1a). They are manipulated individually by tightly focused laser beams. The qubit states are formed by two specific internal states of each ion ($|g\rangle$ and $|e\rangle$) and are 'dressed' by the oscillator states $|n\rangle$ of the ion's motion. The advantages of using ions are the long coherence times (~ 10 min) and the high initialization and detection efficiency of the qubit state ($> 99\%$). Furthermore, through the mutual Coulomb repulsion the ions' internal qubit state can be linked with the external motion of the ions [3]. This is accomplished by applying qubit state-dependent optical or microwave dipole forces on the ions. By scaling beyond 50 qubits the trapped ions can be shuttled through space. The initially separated chains of ions can be coupled in a multiplexed architecture called the quantum charge-coupled device (QCCD). To go even beyond 1000 qubits separate registers of ion chains need to be linked with photonic interfaces, i.e. chains of ions are entangled with each other using propagating photons emitted by a subset of ions from each register [3]. Another approach which does not rely on photonic interconnections and their limited rate is based on today's silicon semiconductor and ion trap technology [4]. The basic idea is the same as QCCD where ions are shuttled by RF and static voltage electrodes. The connection between different modules does not rely on photonic interfaces but on fast ion transport between adjacent modules. The challenge is to fabricate RF and static voltage electrodes all the way to the edges

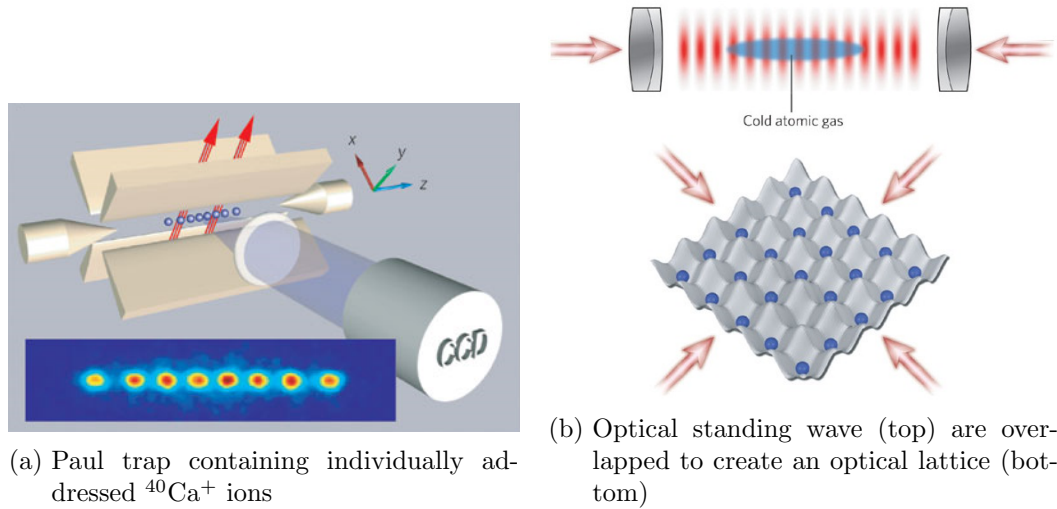


Fig. 1.1: Trapped, laser-cooled atomic ions and ultracold, neutral atoms in an optical lattice. a.) Paul trap (beige) containing individually addressed $^{40}\text{Ca}^+$ ions (blue). After cooling by laser beams (red), the trapped ions form a string and are then imaged by using a charge-coupled device (CCD). In the CCD image the spacing of the two centre ions is $\sim 8\ \mu\text{m}$. (image taken from [2]) b.) An optical standing wave is generated by superimposing two laser beams (top) creating a periodic array of microscopic laser traps. By overlapping several standing waves higher-dimensional optical lattices can be formed (bottom). (image taken from [5])

so that the electric fields reach beyond the edges and align two neighbouring modules accurately in order to create overlapping electric fields. However, creating large trapped ion arrays in reality is incredibly involved as a very large number of RF and static voltage electrodes needs to be controlled individually. Moreover, laser beams must also be applied in several locations simultaneously, which increases the laser requirements drastically.

Ultracold atoms in optical lattices [5] cannot yet rival the precise control of atomic ion traps, but show very promising features. On the one hand neutral atoms couple more weakly to the environment than ions resulting in long storage and coherence times, even in the proximity of bulk materials. On the other hand ultracold atoms in optical lattices allow to initialize a large number of particles simultaneously, which is needed for quantum computation. The optical lattice is formed by interfering laser beams propagating along different directions resulting in a periodic pattern of bright and dark fringes in one, two or three dimensions (see Fig. 1.1b). Ultracold atoms loaded in the optical lattice are sorted in such a way that every lattice site is occupied by a single atom due to strong repulsive interaction in case of bosons or due to the Pauli blocking in case of fermions, but this site filling mechanism is not reliable, i.e. not every site is filled with an atom. The spin states (e.g. $m_F = 0$ and $m_F = -1$) of these loaded, ultracold atoms are used as the logical qubits and can be manipulated using radio-frequency waves. However, controlling and imaging a single atom in an optical lattice is a huge challenge. One way of addressing a single atom in an optical lattice is described in [6]. Two circularly polarized laser beams are crossed at a right angle and cause a vector light shift on the $m_F \neq 0$ levels. This vector

light shift is about twice as large for the targeted atom as for any other. The addressing beams can be directed to a new target by using micro-electromechanical-system mirrors. By scanning the microwave frequency which transfers the atom between the qubit states a shift of the resonance frequency of the atoms along the addressing beams as well as for the atoms at the crossing of the addressing beams is observed. By transferring only the 'cross' atoms with the microwave the targeted atoms can be made optically visible. However, in order to achieve scalable neutral atom quantum computation the following issues among others need to be resolved: scalable addressing for two-qubit gates, reliable site filling and the implementation of error correction. Moreover, the heating of the whole system due to laser beams or moving the atoms close together to initiate quantum gates needs to be dealt with.

Rydberg atoms [7] are highly excited neutral atoms (quantum number $n \gg 1$). Lattices containing Rydberg atoms have similar advantages and disadvantages as ground-state neutral atoms, but the large improvement is that the two-atom interaction can be turned on and off with a contrast of twelve orders of magnitude (see Fig. 1.2a). This can be compared to the interaction strength of trapped ions, whose Coulomb interaction is much stronger but always present making it difficult to establish a many-qubit register. However, transferring a neutral atom to a Rydberg state requires either a one photon excitation with deep UV wavelength (~ 297 nm) or a two photon excitation via the first resonance level, which requires well-stabilized lasers. Furthermore the lattice spacing is constrained by the requirement that a Rydberg excited electron with a characteristic orbital radius $\sim a_0 n^2$, where a_0 is the Bohr radius, should not collide with neighbouring ground-state atoms. Lastly, the strong dipole-dipole interaction not only improves the lifetime of the Rydberg state and hence the coherence time, but also makes it extremely sensitive to small low-frequency magnetic fields.

Superconducting circuits [8] are macroscopic in size but have quantum properties like quantized energy levels, superposition of states and entanglement. The superconducting qubit is realized by either the magnetic flux, the electric charge or the phase difference across a Josephson junction controlled by electromagnetic pulses. The underlying superconducting properties are flux quantization and Josephson tunnelling. The magnetic flux in a ring, which gets cooled to superconductivity while a magnetic field is applied, is quantized after the magnetic field is switched off (see Fig. 1.2b). A Josephson junction consists of two superconductors separated by an insulating barrier of ~ 2 nm through which Cooper pairs can tunnel coherently. The advantages of these circuits are that they can be engineered to be isolated from the electrical environment, although they are of macroscopic scale, and are thus represented by a single degree of freedom. Neighbouring superconducting qubits naturally couple to each other either capacitively or inductively [1]. Although this coupling can be used for simple quantum logic gates, one needs to have long distance interaction and switch the interaction on and off in order to create large-scale quantum computer architecture. Microwave photons in transmission lines allow two-qubit gate operations within a few tens of nanoseconds and measurements of non-local quantum correlations between qubits that are several millimetres apart. Moreover, the ability to design and structure these qubits arbitrarily to tailor their characteristic frequencies among other parameters is a great advantage over atoms. However, superconducting qubits need to be created by electron-beam lithography, operated at mK temperature in an ultralow-noise

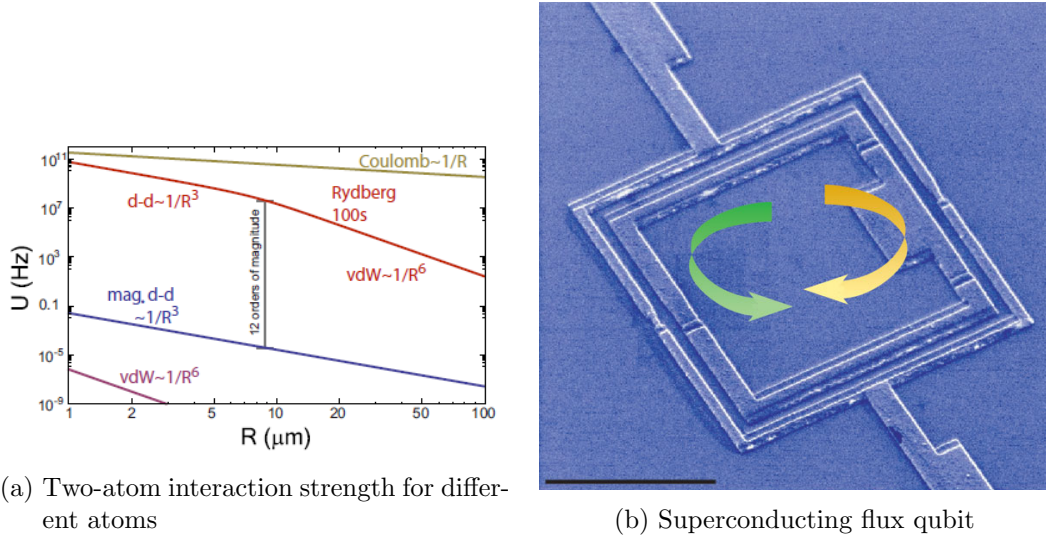


Fig. 1.2: Rydberg atoms and superconducting qubits. a.) The dependence of the two-particle interaction strength on separation R for singly charged ions (yellow), ground-state Rb atoms (blue, violet) and Rb Rydberg atoms $n = 100s$ (red) is depicted. At the characteristic length scale R_c where the Rydberg atoms change there separation dependence the ratio between Rydberg interaction and ground-state is approximately 10^{12} . (image taken from [7]) b.) A flux qubit consists of a superconducting loop interrupted by three Josephson junctions. The arrows indicate the current flow in the two qubit states (green - $|\uparrow\rangle$ and yellow - $|\downarrow\rangle$). (image taken from [8])

environment, as decoherence remains the biggest challenge for superconducting qubits, and measured using highly sensitive techniques.

Quantum computing with single atoms in vacuum brings with it the complication that the atoms need to be cooled and trapped, while superconducting qubits still mostly struggle with rather short decoherence times and require cooling to mK temperatures [1]. To create a large array of qubits, 'single atoms' can be integrated into a solid-state host. The requirements for implementation of a solid-state spin-photon interface are the presence of an impurity with a degenerate ground-subspace coming from spin degrees of freedom and optical transitions to excited states with strong spin-orbit coupling [10]. One of the possible realizations are quantum dots, which are mesoscopic semiconductor structures. Quantum dots come in many varieties. There are electrostatically controlled quantum dots, where the motion of the electron and/or hole are confined by controlled voltages, and self-assembled quantum dots, where a random semiconductor growth process creates the potential for confining electrons and/or holes [10]. The latter often exhibit discrete optical spectra and are therefore of greater interest for spin-photon interfaces. However, a problem of self-assembled quantum dots is that they form in random locations, their optical characteristics vary from dot to dot and their coherence times are only a few nanoseconds or a few microseconds using spin echo sequences. Fortunately, these quantum dots are optically initialized very fast and allow for single spin control via ultrafast pulses (on the

order of picoseconds), which might enable extremely fast quantum computers.

Last but not least of the promising candidates of quantum computing is the nitrogen-vacancy centre (NV) in diamond [11]. The NV is a point defect in diamond consisting of a substitutional nitrogen-lattice vacancy pair. Its axis is oriented along the $\langle 111 \rangle$ crystalline direction and it has a C_{3v} symmetry. The NV exists in two charge states: the neutral nitrogen-vacancy centre (NV^0) and the negative nitrogen-vacancy centre (NV^-). The latter has been a candidate for many studies and thus is much better understood, although many properties are still not resolved. The NV^- can be identified either by its zero phonon line at 1.945 eV (637 nm) and associated vibronic bands that extend to higher/lower energy in absorption/emission or by a zero field magnetic resonance at ~ 2.88 GHz between the $m_s = 0$ and $m_s = \pm 1$ spin sub-levels of the spin triplet ground state. The NV^- fluoresces strong enough to be detected as single centre using scanning confocal microscopy. Furthermore, it is extremely photostable under off-resonance excitation and shows no sign of photobleaching except in extreme conditions. The ground state spin has the longest single spin coherence time ($T_2 = 1.8$ ms) at room temperature of any electronic spin in a solid, which can be used to couple to proximal electronic and nuclear spins and to manipulate these spins.

The NV^- was identified as a possible solid state qubit suitable for quantum information processing because of the possibility to optical prepare and read out the centre's electronic spin. Moreover, demonstrations of NV^- - NV^- spin coupling as well as steps towards photonic coupling speak for its scalability. The readout of the NV^- spin is enabled by the differing fluorescence of the $m_s = 0$ and the $m_s = \pm 1$ spin projections due to different non-radiative decay pathways. Additionally, these non-radiative transitions also provide the mechanism for optical spin preparation. After few optical cycles the probability to find the NV^- in the $m_s = 0$ spin state is higher than for finding it in the $m_s = \pm 1$ spin states, a process known as optical spin polarisation. Both effects, optical readout and spin-polarisation, happen simultaneously. However, the degree of ground state optical spin polarisation is not consistently reported and ranges from 42 %-96 %. Unfortunately, the ground state spin-polarization represents the preparation fidelity of the qubit and in order to use the NV^- as a qubit the preparation fidelity has to be well characterised. A second problem is the readout contrast due to low collection efficiencies of current apparatus. A single qubit operation has to be performed many times to distinguish between the different NV^- spin states at room temperature.

After raising some issues of NV^- s as qubits their advantages are summarized as follows:

- A bright photostable optical transition, that can be used for detection of single NV^- s and single photon generation
- An optical zero-phonon line at room temperature that is independent to electric and strain fields and dependent to the magnetic fields (Zeeman effect)
- A magnetically resonant and controllable electronic spin that exhibits long coherence times and enables coupling to close spins
- Optical spin-polarisation and readout of the spin state
- Flexibility and robustness in fabrication

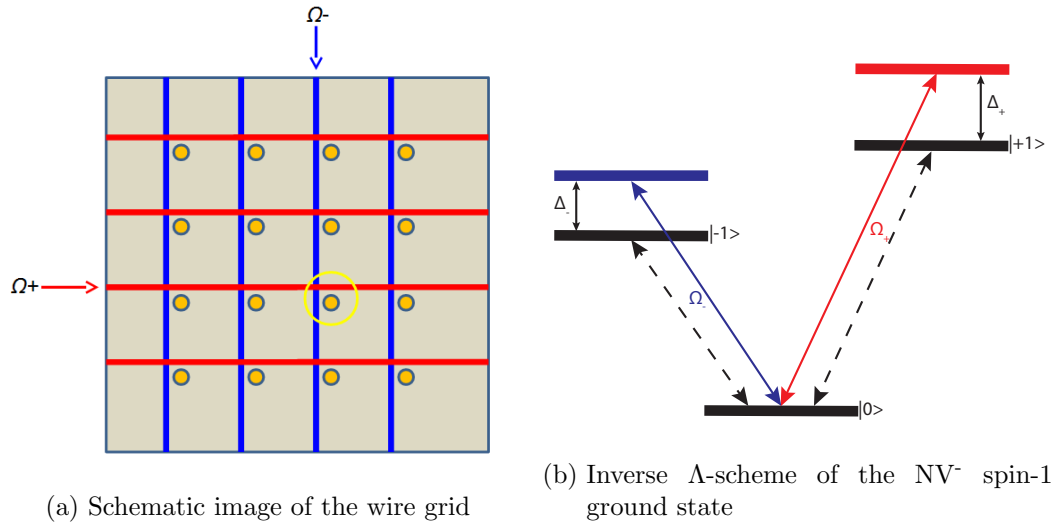


Fig. 1.3: Principle of operation of the wire grid using a STIRAP-inspired transfer sequence. a.) Schematic image of the wire grid. By sending one MW pulse (Ω_+ , red) through a vertical wire and the other MW pulse through a horizontal wire (Ω_- , blue) the condition for a transfer between $|-1\rangle$ and $|+1\rangle$ is only fulfilled at the junction of both wires (yellow circle). The yellow dots depict the sites of a NV qubit. b.) The blue line is the driving field Ω_- with a detuning Δ_- of the $|0\rangle \Leftrightarrow |-1\rangle$ transition, while the red line is the driving field Ω_+ with a detuning Δ_+ of the $|0\rangle \Leftrightarrow |+1\rangle$ transition. The dashed arrows indicate resonant transitions.

The NV^- is not only a promising candidate for quantum information processing, but can also be used as a nanoscale sensor for DC, AC and fluctuating magnetic and electric fields as well as a high sensitivity thermometer. In this thesis the main aspect lies upon demonstrating a scalable system of qubit control using NV^- s.

1.2 Scalable qubit control

Control over individual qubit in large-scale quantum systems is a requirement for many quantum technologies. In case of a two-dimensional array of magnetic spin qubits the difficulty consists in accessing each qubit with control lines, limiting the possibility to scale the quantum system. In case of NVs a grid of wires (see Fig. 1.3a) in combination with a STIRAP-inspired transfer sequence (see Fig. 1.3b) can address individual qubits. The STIRAP-inspired transition transfers the NV^- from $|-1\rangle$ to $|+1\rangle$, which requires two MW pulses (Ω_- and Ω_+). By sending one MW pulse through a vertical wire and the other MW pulse through a horizontal wire the condition for a transfer between $|-1\rangle$ and $|+1\rangle$ is only fulfilled at the junction of both wires. A single qubit can be addressed using this method.

However, as this method has not been tested yet, the performance of the wire grid can be anticipated by using a single wire with a single NV, as single wire measurements are

easier to control and better understood. Using a single wire and a single NV (see Sec. 5.2), the dependence on the MW power of the two-tone efficiency is of great importance as the power of the MW pulse depends strongly on the distance to the wires, which is crucial for the application with the wire grid. Moreover, as the MW pulses do not only affect the single site at the junction but also sites along the wires, the time-behaviour of the two-tone transfer as well as the Rabi nutation is observed. Varying the detuning of the two-tone pulses affects the two-tone transfer and the Rabi nutation differently and hence, detuned two-tone pulses can be used to avoid unintended transitions. After getting a good estimate of the performance of the wire grid the grid itself is implemented in the experimental setup (see Sec. 5.3). Measurements confirm the expected performance and the possibility to address a single site without affecting any other sites.

If detuned two-tone pulses are still not sufficient to avoid unintended transitions, the MW signal from the two-tone pulse sequence can be cancelled by using a counteracting signal in a neighbouring wire. The effects of counteracting pulses are demonstrated performing a Rabi nutation measurement where the phase between signal and counter-signal is shifted resulting in cancellation of the oscillation at a relative phase shift of π . By implementing counteracting signals the wire grid can be built smaller while maintaining high performance qubit control.

2 Basic physics of the NV centre

In this chapter I will discuss the basic physics of the nitrogen vacancy centre (NV). I will begin by explaining the physical structure of the NV briefly (Sec. 2.1) - note that I will restrict myself to the negatively charged NV centre (NV⁻) for the rest of this thesis, unless otherwise noted. This will be followed by the most important optical transitions (Sec. 2.2). After discussing the NV⁻-specific description of the fine- and hyperfine structure (Sec. 2.3) I will consider non-unitary dynamics, which result in dephasing and loss of coherence (Sec. 2.4). As many fundamental qualities of the NV can already be described with a two-level quantum model, I will explain the most important features of the two-level model (Sec. 2.5). Lastly I will introduce the principles of a three-level model (inverse- Λ -scheme) as the final goal of this thesis is to perform three-level manipulations (Sec. 2.6).

2.1 Structure of the NV centre

There are many colour defects in diamond, but the nitrogen-vacancy defect (NV) is one of the most prominent ones, especially in nitrogen-rich diamonds. Furthermore the NV has several advantages compared to other colour defects: Two of the main advantages are that on the one hand green laser light initializes the NV in the ground state and on the other hand its spin state can be read out optically, which allows for easy detection (see Sec. 2.2). Additionally the NV has a long T_2 decoherence time even at room temperature (see Sec. 4.2.3), which can be used to perform long and complicated measurement schemes.

The NV is formed by substituting a carbon atom with a nitrogen atom and an adjacent vacancy (see Fig. 2.1). The orientation of the NV axis is the $\langle 111 \rangle$ direction [12] and therefore four crystallographically equivalent orientations of this NV axis in diamond are possible. As the vacancy is surrounded by three carbon atoms in nearest-neighbour positions, the defect has a C_{3v} symmetry, meaning that the electronic states are characterized by their transformations under C_{3v} symmetry operations.

NVs are produced by implanting nitrogen in diamonds and then irradiating these diamonds with electrons, neutrons or various ions in order to create vacancies. Secondly annealing with a temperature over 650°C (activation energy of about 1.7 eV) allows the vacancies to become mobile (diffusion length of about 260 nm [14]) until they get trapped by the nitrogen atoms. Samples with single NVs are produced by using ultra pure diamonds, in which NVs occur naturally. Further details on the creation and properties of NVs can be found in references [15] and [16].

2.2 Term scheme and optical transitions

Each of the nearest-neighbour carbon atoms and the nitrogen atom contribute one dangling bond orbital to the centre. These orbitals have to be filled up with electrons according

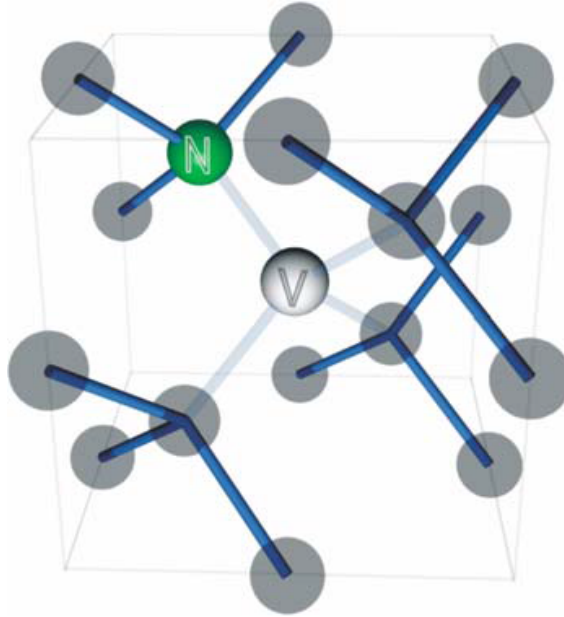


Fig. 2.1: Structure of the NV consisting of the nitrogen atom (green) and the adjacent vacancy (white). The vacancy has three carbon atoms as nearest neighbours leading to C_{3v} symmetry of the defect. (image taken from [13])

to Hund's rule. Each carbon atom gives one electron, the nitrogen atom contributes two. This object is electrically neutral and is called NV^0 . However, a sixth electron, which is most likely taken from other nitrogen impurities, can bind to the defect, forming a negatively charged NV, called NV^- .

The best way to describe the electronic structure of the defect is given by the 'linear combinations of atomic orbitals' (LCAO) approach [17], which delivers a qualitative model of the defect, but contains a number of phenomenological parameters. The exact electronic structure, however, is still a partially unsolved problem.

The LCAO approach of the C_{3v} symmetry delivers possible computable orbits [18]. The irreducible representations of the many-electron states correspond to the orbitals of the electrons. The ground state and many excited states can be found, but only the ground state and three further excited states are considered as these are the only ones important for this thesis. Furthermore all experiments are carried out at room temperature, where phonon processes take place, which average out the orbital branches in the excited state [19], resulting in a quite simple term scheme (see Fig. 2.2).

The ground state 3A_2 is a spin triplet times an orbital singlet state, which is symmetric under rotation and changes sign under reflection. This spin triplet state is split by the spin-spin interaction (zero-field splitting) in one $m_s = 0$ and two $m_s = \pm 1$ states, which are separated by 2.88 GHz. The optical excited state 3E is a spin triplet times an orbital doublet state and has a lifetime of about 10 ns. The spin singlet states 1A_1 as well as 1E_1 do exhibit energies in between of the previous two. 1A_1 is symmetric along the principal NV axis and is a metastable state with a lifetime of about 220 ns at room temperature to 460 ns at 4.4 K. 1E_1 is a spin singlet times orbital doublet state with a very short lifetime

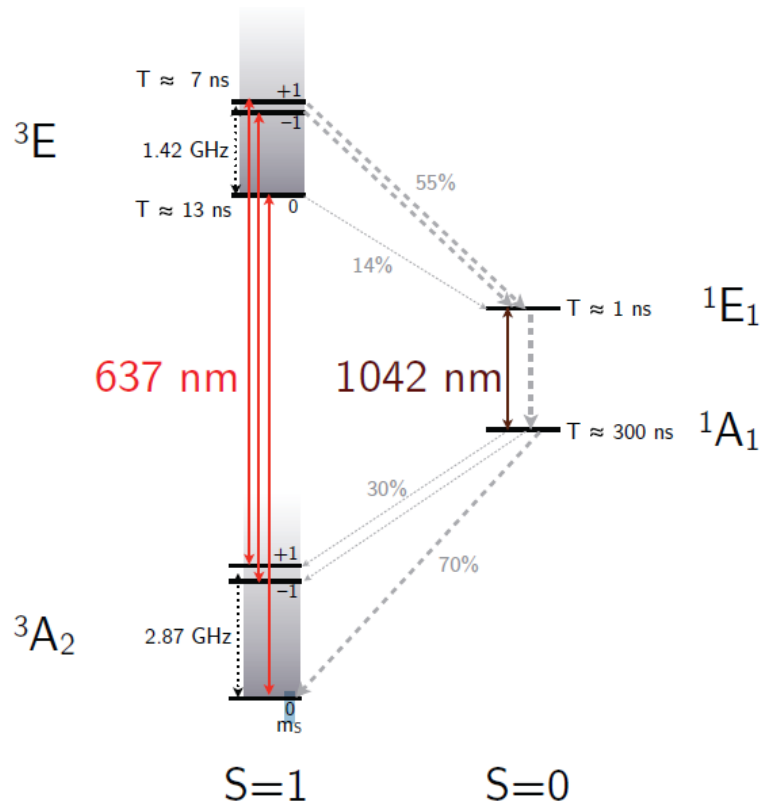


Fig. 2.2: Term scheme of NV at high temperature. Electric dipole transitions are indicated as solid (dark) red arrows, magnetic dipole transitions as dotted black arrows. Nonradiative intersystem crossing transitions are shown as dashed grey arrows, the approximate branching ratios from the initial level are indicated as percentages and arrow thicknesses. Note also the level lifetimes and spin projection quantum numbers [20].

<1 ns and thus not very important for further considerations [20].

2.2.1 Optical transitions

The optical transitions have to obey Fermi's golden rule. There are four dipole-allowed transitions in the term scheme of Fig. 2.2, which do not involve vibrational excitations, i.e. zero-phonon-lines (ZPL). Between the ground triplet-state 3A_2 and the excited triplet-state 3E are three spin-preserving transitions at a wavelength of 637 nm (1.945 eV), whereby the probability of a spin-flip at room temperature is about 1% of the allowed transition rates [21]. The final optical allowed transition is between the two singlet levels 1A_1 and 1E_1 at 1042 nm (1.940 eV) [20]. As the much weaker 1042 nm line is not used in our experiment, the 637 nm line will be referred to as the NV⁻ ZPL. Additionally there are non-radiative transitions, shown as dashed grey arrows in Fig. 2.2.

Furthermore, phonons cannot be neglected as the NV⁻ also couples quite strongly to local and bulk vibrations, especially the optically excited states. Therefore only about 3%

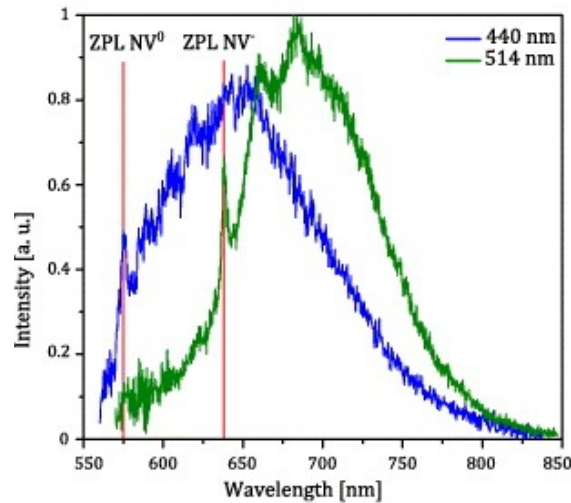


Fig. 2.3: Emission spectra of the NV^0 and NV^- at room temperature. The excitation wavelength were chosen so that one only excites NV^0 and the other only NV^- . Spectra are normalized to the same area. (image taken from [22])

of the fluorescence intensity is emitted into the ZPL, the rest is emitted into the phonon side band (PSB) [22] (see Fig. 2.3), resulting in wavelengths of the fluorescence light larger than 637 nm. Although it is somewhat inconvenient that most of the fluorescence is in the PSB, it can be used for off-resonant excitation with wavelengths shorter than the ZPL, as vibrational energy states also exist above the optical excited states. With blue-detuned excitation the defect is excited to its optically excited states plus phonons, which then decay rapidly (\sim ps) and non-radiatively to the excited states. This has the advantage, that the exact wavelength of the laser does not have to be monitored, because inaccuracies of several nanometers do not matter.

2.2.2 Spin polarization and fluorescence time traces

One of the reasons why NV^- s are such promising candidates for quantum information processing are the experimentally quite simple spin-dependent optical dynamics, which can be used to initialize and readout the spin using non-resonant excitation and broadband fluorescence detection. As stated previously the optical transitions between the triplet states 3A_2 and 3E are spin conserving with a probability of less than 1% for a spin-flip. However, there is a process in the cycle which can lead to spin-flips namely the inter-system crossing (ISC) process. The $m_s = \pm 1$ sublevels of the excited triplet state preferentially undergo non-radiative transitions to the two singlet states (see Fig. 2.2), where the lower one 1A_1 is a metastable state with a lifetime of about 300 ns and preferentially decays non-radiatively to the $m_s = 0$ sublevel of the ground state. As ISC occurs mainly for $m_s = \pm 1$ of the 3E state a spin-flip happens providing a mechanism for spin initialization into the $m_s = 0$ ground state by off-resonant optical pumping. After a few optical cycles ($\sim 3 \mu s$) more than 80% of the spins are polarized in $m_s = 0$ (average quoted spin-

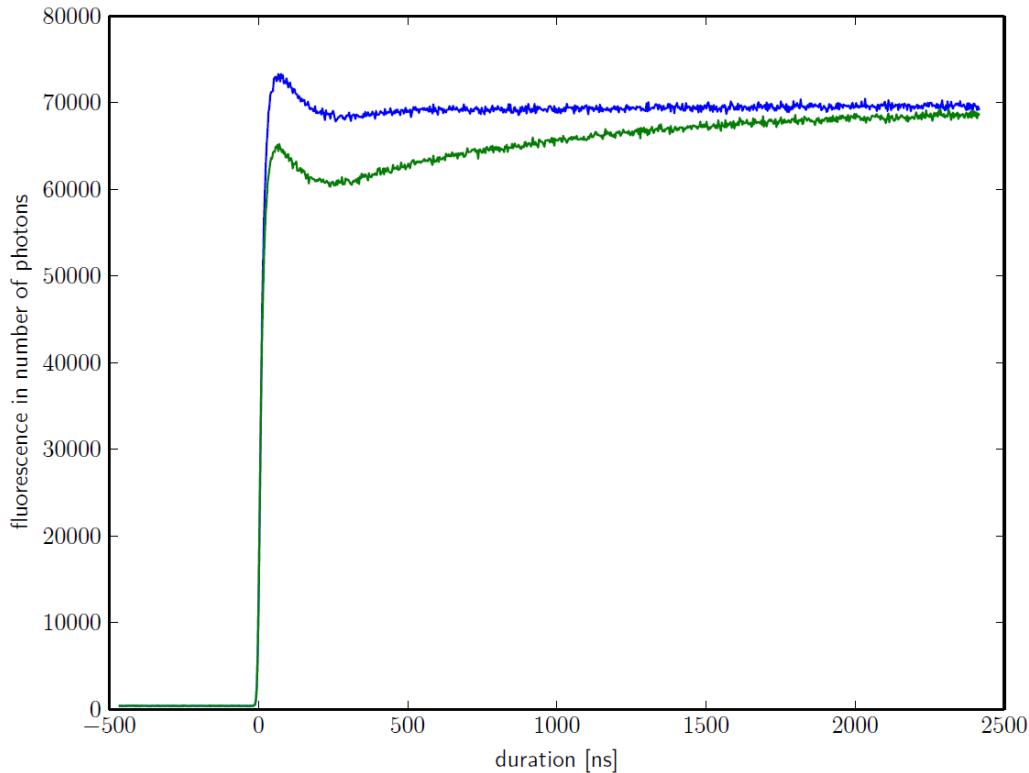


Fig. 2.4: Fluorescence time trace under constant illumination. The blue trajectory is the bright state $m_s = 0$, whereas the green trajectory represents the dark state $m_s = -1$. The area, which is spanned by the difference between the time trace of the bright and the dark state, represents the signal that allows to discriminate different spin state. (image taken from [23])

polarisation from the vast range of spin-polarisations reported [11]). Additionally as 1A_1 is a metastable state, the spin is trapped and cannot undergo additional optical cycles resulting in remaining dark.

With the dynamics described previously, a way to distinguish the spin state of the system is available. Experimentally this is realized by measuring the fluorescence time traces under illumination (see Fig. 2.4). If the system is initially in the $m_s = 0$ state, an intensity peak immediately after the start of the illumination is detected decaying to equilibrium. For an initial state in $m_s = \pm 1$ the time trace looks different. There is a drop of the intensity 'peak' immediately after the start of the illumination below the equilibrium level, which happens due to trapping of the electron in the metastable state. After decaying for roughly 300 ns both fluorescence time traces return to equilibrium after a few μs . By integrating over a lot of sweeps the fluorescence time traces are smoothed out, and it is possible to determine the spin state by comparing the initial fluorescence with the fluorescence in equilibrium. These level dynamics are the basis of the optically detected magnetic resonance (ODMR) technique and all following pulsed measurements (see Sec. 4.1 and Sec. 4.2).

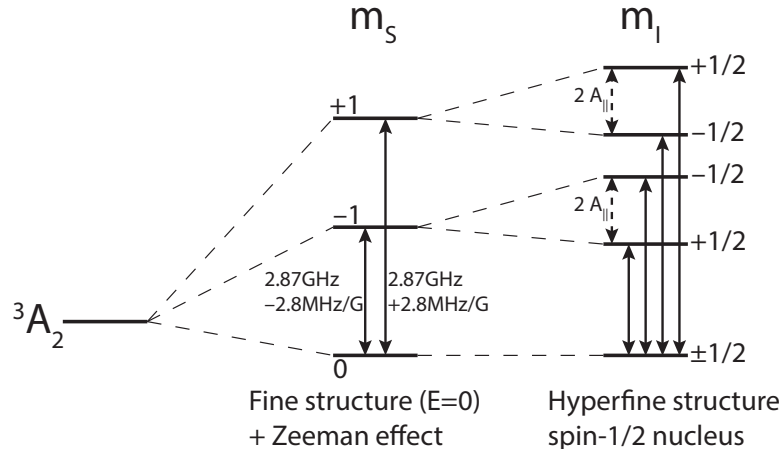


Fig. 2.5: Term scheme of the NV^- ground state fine- and hyperfine structure due to coupling to a spin- $\frac{1}{2}$ nucleus on a nearest-neighbour lattice sites (possibly ^{13}C or ^{15}N). There is no strain and an external magnetic field lifts the degeneracy of the $m_s = \pm 1$ states. Solid arrows indicate magnetic dipole transitions.

2.3 Fine- and hyperfine structure

As explained in the previous section, the optical ground- and excited states are only used to read out the spin state of the system. Therefore the spin sublevels ($m_s = 0, \pm 1 - |0\rangle, |+1\rangle$ and $|-1\rangle$ respectively) of the ground state are the quantum bit (qubit) levels used in the experiment, and thus the fine- and hyperfine structure of the ground state play an important role to understand the dynamics of the NV^- . Furthermore quantum information is stored and processed in these spin sublevels and as bulk phonons couple rather weakly to the spins the system exhibits a surprisingly long coherence time even at room temperature [24], i.e. dephasing is not limited by coupling to phonons, but by coupling to other spins in the surrounding spin bath.

As mentioned before in the absence of external fields the degeneracy of $|0\rangle$ and $|\pm 1\rangle$ levels of the optical ground and excited state are lifted due to spin-spin interaction of the two unpaired electrons (zero-field splitting - ZFS). Additionally the degeneracy of $|-1\rangle$ and $|+1\rangle$ is abrogated by slightly breaking the C_{3v} symmetry of the NV^- with a non-axial strain field created by imperfection of the diamond lattice. In order to split $|\pm 1\rangle$ further the Zeeman effect can be used by applying a magnetic field, ideally along the NV^- axis (28 MHz/mT). Thus the qubit states used to store quantum information are the transitions from the $m_s = 0$ state to either the $m_s = -1$ or $m_s = +1$ state.

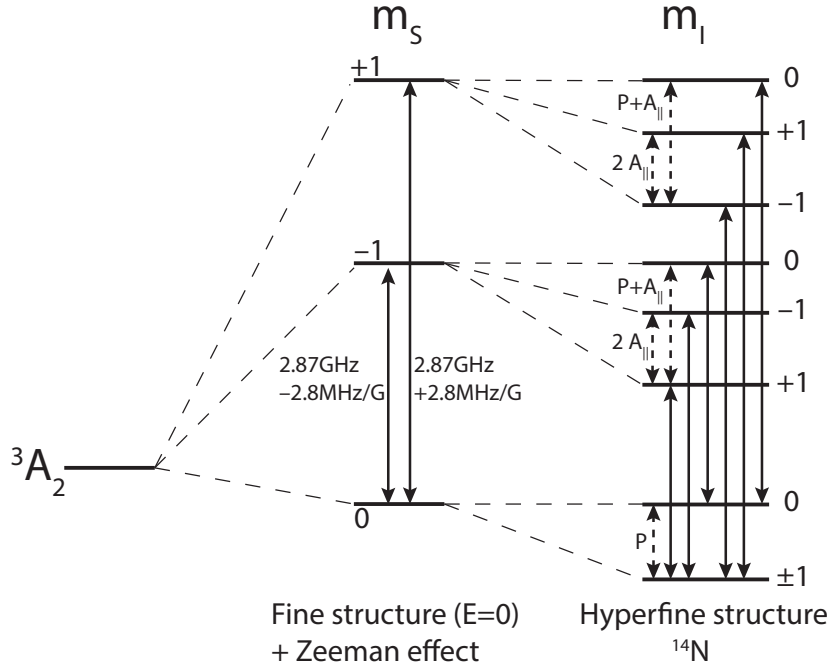


Fig. 2.6: Term scheme of the NV^- ground state fine- and hyperfine structure due to coupling to ^{14}N . There is no strain and an external magnetic field lifts the degeneracy of the $m_s = \pm 1$ states. Solid arrows indicate magnetic dipole transitions. Parameters as given in the main text.

The last contribution to the NV^- -Hamiltonian is the coupling of the electron spin to the nuclear spin of the ^{14}N atom next to the vacancy (see Fig. 2.6) and possibly to spin- $\frac{1}{2}$ nucleus (^{13}C atom - natural abundance of 1.1% [25] - or ^{15}N) shown in Fig 2.5) in the neighbouring lattice sites:

$$\begin{aligned}
H_{GS} &= H_{ZFS} + H_{Zeemann} \\
&+ H_{HF}^N + H_{HF}^C \\
&+ H_{nucl.quadrapole}^N + H_{nucl.Zeemann}^N + H_{nucl.Zeemann}^C \\
&= D[S_z^2 - \frac{1}{3}\mathbf{S}(\mathbf{S} + 1)] + \mu_B g_e \mathbf{S} \cdot \mathbf{B} \\
&+ A_{\parallel}^N S_z I_z^N + A_{\perp}^N (S_x I_x^N + S_y I_y^N) + A_{\parallel}^{\frac{1}{2}} S_z I_z^{\frac{1}{2}} + A_{\perp}^{\frac{1}{2}} (S_x I_x^{\frac{1}{2}} + S_y I_y^{\frac{1}{2}}) \\
&+ P[I_z^{N^2} - \frac{1}{3}\mathbf{I}^N(\mathbf{I}^N + 1)] + \mu_B g_N \mathbf{I}^N \cdot \mathbf{B} + \mu_B g_{\frac{1}{2}} \mathbf{I}^{\frac{1}{2}} \cdot \mathbf{B}
\end{aligned} \tag{2.1}$$

where $D = 2.88$ GHz is the ZFS and \mathbf{S} and \mathbf{I} are the electron and nuclear spin operators, respectively. \mathbf{B} denotes the external magnetic field and μ_B is Bohr's magneton. The interaction between ^{14}N nuclear spin and the electron spin are given by an axial and transversal term, $A_{\parallel}^N = 2.3$ MHz and $A_{\perp}^N = 2.1$ MHz [11], whereas the coupling of the electron spin to the nuclear $\frac{1}{2}$ -spin ($A_{\parallel}^{\frac{1}{2}}$, $A_{\perp}^{\frac{1}{2}}$) depends on the position of the atom with respect to the NV^- (e.g. ^{13}C - 126 MHz for nearest-neighbour and few MHz for nuclei

further away [25]). The strong quadrupole coupling of $P \simeq 5$ MHz splits the $m_N = 0$ state and the $m_N = \pm 1$ states of the ^{14}N nucleus [26]. g , g_N and $g_{\frac{1}{2}}$ are the respective gyromagnetic ratios.

If perturbations due to non-axial magnetic fields are not too strong the quantization axis points along the NV axis, otherwise there may be some mixing of the levels. Lastly, the Stark effect due to electric fields is several orders of magnitude smaller than the Zeeman effect and can be neglected with regard to the experiment in this thesis (not included in Eq. 2.1).

2.4 Dephasing and decoherence

Up to this point only unitary dynamics have been considered. In reality however non-unitary dynamics need to be taken into account, like spontaneous emission in the excited state or small phase shifts due to slightly different magnetic environment for each qubit. These processes are characterized by three time constants: T_1 is the longitudinal (spin-lattice) relaxation time, T_2 is the transverse (spinspin) relaxation time and T_2^* is due to inhomogeneous broadening [27].

The T_1 relaxation processes are the simplest to understand and happen due to decay mechanisms of the excited state to the ground state as a result of spontaneous emission, interactions with phonons or other spin-flipping processes. The decay processes occur stochastically and randomly break the coherence of the wave function. T_1 is thus governed by the lifetime of the excited state and ranges from few nanoseconds for optical transitions to many minutes in nuclear magnetic resonance.

The T_2 decoherence processes are more subtle to understand and generally T_2 is the time constant describing homogeneous broadening. However T_2 is more often referred to as spin-spin relaxation time. The loss of coherence is due to coupling of the qubit spins to its local spin environment and happens on a timescale of T_2 , which is individual for each spin system. In the case of a single qubit T_2 describes the loss of the phase relation between the two basis states in a superposition state. In order to measure T_2 a spin-echo sequence is used (see Sec. 4.2.3), where the time constant defining the decay of the envelope corresponds to T_2 .

The T_2^* decoherence processes have different explanations considering ensembles and single qubits. In an ensemble of spins the phase relations between individual qubits can get lost on a timescale of T_2^* due to their slightly different intrinsic resonance frequencies (inhomogeneous broadening) or extrinsic source of spectral drift like inhomogeneities of the magnetic field. In single qubits T_2^* refers to the timescale of dephasing that is reversible (e.g. by inverting the system or the bath), in contrary to T_2 , which describes irreversible decoherence processes, in a given experimental context. There are two different ways to obtain T_2^* : On the one hand ODMR-spectra (see Sec. 4.1) with decreasing MW power are recorded and the obtained linewidth is extrapolated at zero MW power, where the FWHM then gives T_2^* according to

$$T_2^* = \frac{1}{\pi\Gamma_{FWHM}}. \quad (2.2)$$

On the other hand a Ramsey-type measurement is performed (see Sec. 4.2.2), where the

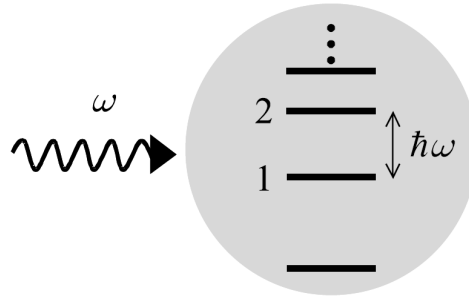


Fig. 2.7: The two-level approximation. A transition between the two levels takes place, when the frequency of the driving field coincides with the transition frequency of the system (see Eq. 2.3). (image taken from [27])

time constant describing the decay of the envelope defines T_2^* .

In case of NV⁻s, T_1 is very long ranging up to several milliseconds at room temperature for single NV⁻s as well as ensembles. Such a long relaxation time can be observed as the lifetime of the excited spin state is rather long and a coupling to spin-flipping phonon-mediated processes is weak. However, for T_2 and T_2^* there is no such general statement possible as the coherence time constants vary strongly from sample to sample and are different for single NV⁻s and (dense) ensembles [23]:

- single NV⁻ in chemically pure diamond (with natural 1.1% abundant ¹³C): The dephasing is limited by the dipolar hyperfine coupling to the ¹³C spin bath.
- single NV⁻ in isotopically pure diamond: The dephasing is limited by external magnetic noise, which results in very long T_2 and T_2^* .
- low-density ensembles of NV⁻s in a nitrogen-rich diamond: The dephasing is dominated by impurities from other spins (P₁ centres)
- high-density ensembles of NV⁻s: The coupling between NV⁻s becomes dominant, reducing T_2 and T_2^* drastically.

2.5 Quantum theory of a two-level system

In a system (like an atom or the NV⁻) the electrons can be in many quantum levels, therefore describing all possible transitions between the levels is quite involved. For starters transitions between only two energy states are described. To make a transition between two levels, a driving field can be applied, e.g. a laser or a microwave signal, which has to satisfy

$$\hbar\omega = E_2 - E_1 \quad (2.3)$$

where ω is the driving frequency, E_2 is the higher energy level and E_1 is the lower energy level (see Fig. 2.7). The multi-level system can be reduced to only two levels, if on the one hand the energy difference between the chosen energy levels differs strongly from the

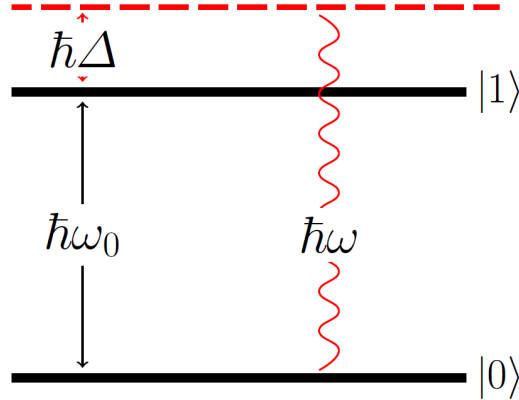


Fig. 2.8: Two-level transition between ground- and excited state ($|0\rangle$ and $|1\rangle$). ω is the frequency of the driving field, ω_0 is the transition frequency and Δ is the detuning. (image taken from [23])

difference between other energy states and if on the other hand the frequency of the driving field is tuned to fulfil Eq. 2.3 and only the transition between those two energy states is driven. This two-level approximation is a valid and powerful model-system capable of describing many fundamental quantum properties.

The two-level system consists of a ground state ($|0\rangle$) and an excited state ($|1\rangle$) forming an orthonormal basis. The ground state in this experiment is the $m_s = 0$ spin-sub-level of the NV^- and the excited state is either the $m_s = +1$ or the $m_s = -1$ spin-sub-level. In the absence of a driving field $|0\rangle$ and $|1\rangle$ are eigenstates of the system with eigenvalues E_0 and E_1 . Solving the undisturbed time-dependent Schrödinger equation $\hat{H}_0|\psi(t)\rangle = i\hbar\frac{\delta|\psi(t)\rangle}{\delta t}$, where \hat{H}_0 is the time-independent Hamiltonian and $|\psi(t)\rangle$ is the wave function, the coherent superposition of the eigenstates can be written as [27]

$$|\psi(t)\rangle = c_0|0\rangle e^{-i\frac{E_0}{\hbar}t} + c_1|1\rangle e^{-i\frac{E_1}{\hbar}t} = c_0|0\rangle + c_1|1\rangle e^{-i\omega_0 t} \quad (2.4)$$

where $E_0 = 0$ and hence $E_1 = \hbar\omega_0$. c_0 and c_1 describe the wave function amplitude coefficients for the two states, where $|c_0|^2$ is the probability of observing the system in the ground state and $|c_1|^2$ in the excited state. As the system has to be in one of the two states, c_0 and c_1 must fulfil the normalization condition $|c_0|^2 + |c_1|^2 = 1$.

In order to make transitions between $|0\rangle$ and $|1\rangle$ a driving field is switched on, which corresponds to a perturbation $\hat{V}(t)$. Therefore the Hamiltonian can be written as $\hat{H} = \hat{H}_0 + \hat{V}(t)$. Since the states $|0\rangle$ and $|1\rangle$ form a complete basis set, it is still possible to write the general state similar to Eq. 2.4 as

$$|\psi(t)\rangle = c_0(t)|0\rangle + c_1(t)|1\rangle e^{-i\omega_0 t} \quad (2.5)$$

Substituting this wave function into the general Schrödinger equation $\hat{H}|\psi(t)\rangle = i\hbar\frac{\delta|\psi(t)\rangle}{\delta t}$ the whole problem reduces to finding the time-dependent behaviour of the coefficients c_0

and c_1 . After simple algebraic operations [27] one obtains

$$\begin{aligned}\dot{c}_0(t) &= -\frac{i}{\hbar} (c_0(t)V_{00}(t) + c_1(t)V_{01}(t)e^{-i\omega_0 t}) \\ \dot{c}_1(t) &= -\frac{i}{\hbar} (c_0(t)V_{10}(t)e^{i\omega_0 t} + c_1(t)V_{11}(t))\end{aligned}\quad (2.6)$$

where $V_{ij}(t) = \langle i|\hat{V}(t)|j\rangle$.

To solve these differential equations, the form of the perturbation $\hat{V}(t)$ has to be taken into account. With a semi-classical approach $\hat{V}(t)$ is the energy shift of a magnetic dipole in a magnetic field [27]

$$\hat{V}(t) = -\boldsymbol{\mu}\mathbf{b}(t) \quad (2.7)$$

with the magnetic moment $\boldsymbol{\mu} = p\mathbf{r}$, where p is the magnetic pole strength and \mathbf{r} is the vector pointing from South to North pole. By arbitrarily choosing the x-axis as the direction of polarisation the magnetic field can be written as $\mathbf{b}(t) = (b_0, 0, 0) \cos(\omega t)$ and hence Eq. 2.7 simplifies to

$$\hat{V}(t) = -\frac{pxb_0}{2} (e^{i\omega t} + e^{-i\omega t}) \quad (2.8)$$

By introducing the dipole matrix element $\chi_{ij} = p\langle i|\hat{x}|j\rangle$ the matrix elements $V_{ij}(t)$ become

$$V_{ij}(t) = -\frac{b_0}{2} (e^{i\omega t} + e^{-i\omega t}) \chi_{ij} \quad (2.9)$$

Since \hat{x} is an odd parity operator and atomic states have either even or odd parities, it follows that $\chi_{00} = \chi_{11} = 0$. Furthermore the dipole matrix element represents a measurable quantity and thus must be real, the off-diagonal entries have to be $\chi_{10} = \chi_{01}$. With these simplifications Eqs. 2.6 reduce to

$$\begin{aligned}\dot{c}_0(t) &= \frac{i}{2}\Omega_R \left(e^{i(\omega-\omega_0)t} + e^{-i(\omega+\omega_0)t} \right) c_1(t) \\ \dot{c}_1(t) &= \frac{i}{2}\Omega_R \left(e^{-i(\omega-\omega_0)t} + e^{i(\omega+\omega_0)t} \right) c_0(t)\end{aligned}\quad (2.10)$$

where $\Omega_R = |\frac{\chi_{01}b_0}{\hbar}|$ is known as the Rabi-frequency .

The solution for these two differential equations provides an understanding of the time-dependent behaviour of the two-level system. A general solution for this problem can not be found, however there are two extreme cases which are simple to solve: the weak-field- and the strong-field limit. Since it is generally required to drive the spin as fast as possible, an approximation for the strong-field limit is provided.

In the strong-field limit two simplifications are made. Firstly the rotating wave approximation neglects all fast oscillating terms $\pm(\omega + \omega_0)$. This is justified by the fact that $\Delta \ll (\omega + \omega_0)$ and hence the fast oscillating terms average to zero on an appreciable time-scale much faster than any observation. Secondly the case of exact resonance $\Delta = \omega - \omega_0 = 0$ is made. By using these simplifications Eqs. 2.10 reduce to

$$\begin{aligned}\dot{c}_0(t) &= \frac{i}{2}\Omega_R c_1(t) \\ \dot{c}_1(t) &= \frac{i}{2}\Omega_R c_0(t)\end{aligned}\quad (2.11)$$

Differentiating $\dot{c}_1(t)$ and inserting it in $\dot{c}_0(t)$ in Eq. 2.11 and vice versa yield two second order differential equations, which can be solved by assuming that the system at $t = 0$ is in the ground state ($c_0(t) = 1$ and $c_1(t) = 0$). The solutions are

$$\begin{aligned} c_0(t) &= \cos\left(\frac{\Omega_R t}{2}\right) \\ c_1(t) &= i \sin\left(\frac{\Omega_R t}{2}\right) \end{aligned} \quad (2.12)$$

and accordingly the time-dependent probabilities to find the electron in one of the two states are

$$\begin{aligned} \mathcal{P}_{|0\rangle}(t) &= |c_0(t)|^2 = \cos^2\left(\frac{\Omega_R t}{2}\right) \\ \mathcal{P}_{|1\rangle}(t) &= |c_1(t)|^2 = \sin^2\left(\frac{\Omega_R t}{2}\right) \end{aligned} \quad (2.13)$$

At $t = \frac{\pi}{\Omega_R}$ the spin is in the upper level, whereas at $t = \frac{2\pi}{\Omega_R}$ it is in the lower state. The spin thus oscillates between the upper and lower level with a frequency of $\frac{\Omega_R}{2\pi}$. This oscillatory behaviour in the strong-field limit are commonly known as Rabi oscillations (see Sec. 4.2.1). When the driving field is not exactly resonant with the transition, Eqs. 2.13 change to

$$\begin{aligned} \mathcal{P}_{|0\rangle}(t) &= 1 - \mathcal{P}_{|1\rangle}(t) \\ \mathcal{P}_{|1\rangle}(t) &= \frac{\Omega_R^2}{\Omega^2} \sin^2\left(\frac{\Omega t}{2}\right) \end{aligned} \quad (2.14)$$

where $\Omega^2 = \Omega_R^2 + \Delta^2$.

2.6 Two-tone control of NV ground state

For many applications and techniques of the NV^- (i.e. ODMR, Rabi oscillation, Hahn-echo measurements, etc. - see Sec. 4.1 and Sec. 4.2) considering only either the transition $|0\rangle \Rightarrow |-1\rangle$ or the transition $|0\rangle \Rightarrow |+1\rangle$ is enough. This system is described as a two-level system (see Sec. 2.5). However, as the NV^- has three sublevels ($m_s = 0, \pm 1$) it can also be described as a three-level system, which opens the way for more precise measurements and new measurement techniques, e.g. creating a transition between the states $|-1\rangle$ and $|+1\rangle$ via the state $|0\rangle$.

Assuming the initially populated state is $|-1\rangle$ and a transfer to $|+1\rangle$ is intended, the most intuitive way is to apply a driving field for the transition $|-1\rangle \Rightarrow |0\rangle$ first and afterwards a field for $|0\rangle \Rightarrow |+1\rangle$. By doing so not only $|-1\rangle$ is populated but also $|0\rangle$, which is not a desired result. In case of this experiment the NV^- spin states of interest are $|\pm 1\rangle$, as the future-oriented goal is to initialize the whole wire grid e.g. in $|-1\rangle$ and transfer NV^- s at certain crossings to $|+1\rangle$, creating a qubit system. Any NV^- s in $|0\rangle$ either do not contribute to this qubit system, hence are 'lost', or even disturb the $|-1\rangle \Leftrightarrow |+1\rangle$ transition e.g. by decreasing the contrast.

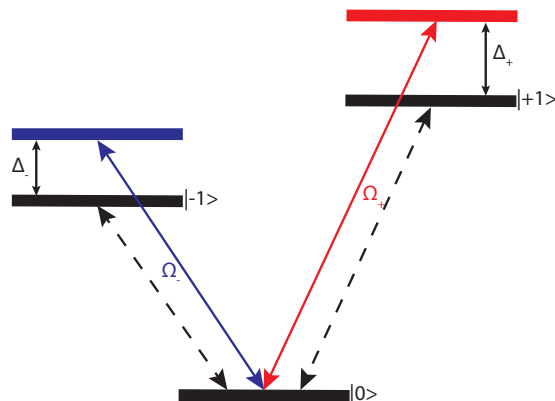


Fig. 2.9: Inverse Λ -scheme of the NV^- spin-1 ground state. The blue (red) line is the driving field Ω_- (Ω_+) with a detuning Δ_- (Δ_+) of the $|0\rangle \leftrightarrow |-1\rangle$ ($|0\rangle \leftrightarrow |+1\rangle$) transition. The dashed arrows indicate resonant transitions.

A more counter-intuitive way at first glimpse is the technique of stimulated Raman adiabatic passage (STIRAP). With STIRAP the driving field $|0\rangle \Rightarrow |+1\rangle$ is applied first and couples the two empty states creating a coherent superposition and thus does not change the population of $|-1\rangle$. By applying the field for $|-1\rangle \Rightarrow |0\rangle$ subsequently the superposition couples to the populated state $|-1\rangle$ creating a 'trapped state' - a state from which the driving field $|-1\rangle \Rightarrow |0\rangle$ cannot transfer population to $|0\rangle$ but only directly to $+1\rangle$ [28].

More importantly the transfer has to be performed smoothly in order to transfer the NV^- from $|-1\rangle$ to $+1\rangle$ adiabatically. By slowly increasing and then decreasing the amplitude of the transfer pulses over time, adiabaticity is granted during the duration of the STIRAP transfer.

The Hamiltonian describing the coupling of the three states by two coherent driving fields is given by [28]:

$$\hat{H} = \frac{\hbar}{2} \begin{pmatrix} 0 & \Omega_+ & 0 \\ \Omega_- & 2\Delta_+ & \Omega_- \\ 0 & \Omega_+ & 2(\Delta_+ - \Delta_-) \end{pmatrix} \quad (2.15)$$

within the rotating wave approximation (RWA) $\omega_{rot} = |\Delta_+ - \Delta_-|$. Ω_{\pm} are the Rabi frequencies of the driving fields, which determine the coupling strength between the states and Δ_{\pm} is the detuning of the driving fields, respectively (see Fig. 2.9). In order for STIRAP to work the two-photon detuning $\delta = |\Delta_+ - \Delta_-|$ has to be zero, which requires that both single-photon detunings are equal ($\Delta_+ = \Delta_- = \Delta$) [29].

The detuning should not be far off resonance from the actual transition and each driving field should only interact with one pair of states ($|0\rangle \leftrightarrow |-1\rangle$ and $|0\rangle \leftrightarrow |+1\rangle$). This demands that the energy-separation of $|\pm 1\rangle$ be large compared to the driving field linewidth or the Rabi frequency - whichever is larger. In our experiment this is realized by applying a magnetic field of $\sim 30\text{mT}$ along the NV axis (see Sec. 2.3).

The eigenstates of the interaction Hamiltonian (Eq. 2.15) can be expressed in terms of

'mixing angles' θ and ϕ , which depend upon the Rabi couplings and the detuning:

$$\begin{aligned}\tan \theta &= \frac{\Omega_-}{\Omega_+} \\ \tan 2\phi &= \frac{\sqrt{\Omega_+^2 + \Omega_-^2}}{\Delta}\end{aligned}\tag{2.16}$$

The eigenstates can then be written as linear combination of the bare states $|-1\rangle$, $|0\rangle$ and $|+1\rangle$:

$$\begin{aligned}|a^+\rangle &= \sin \theta \sin \phi |-1\rangle + \cos \phi |0\rangle + \cos \theta \sin \phi |+1\rangle \\ |a^0\rangle &= \cos \theta |-1\rangle - \sin \theta |+1\rangle \\ |a^-\rangle &= \sin \theta \cos \phi |-1\rangle - \sin \phi |0\rangle + \cos \theta \cos \phi |+1\rangle\end{aligned}\tag{2.17}$$

While the eigenvalue of $|a^0\rangle$ is zero, the eigenvalue of $|a^+\rangle$ is shifted up and of $|a^-\rangle$ down:

$$\begin{aligned}\omega^+ &= \Delta + \sqrt{\Delta^2 + \Omega_+^2 + \Omega_-^2} \\ \omega^0 &= 0 \\ \omega^- &= \Delta - \sqrt{\Delta^2 + \Omega_+^2 + \Omega_-^2}\end{aligned}\tag{2.18}$$

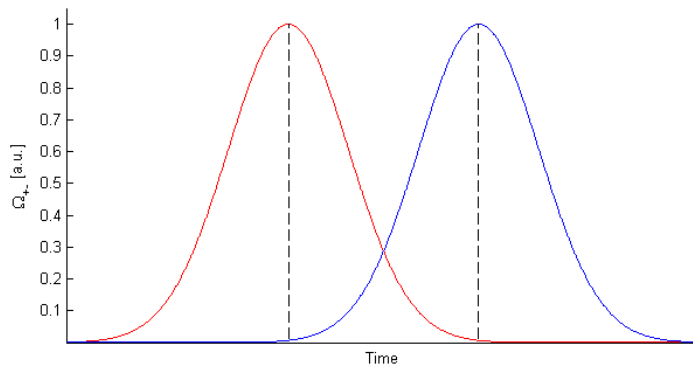
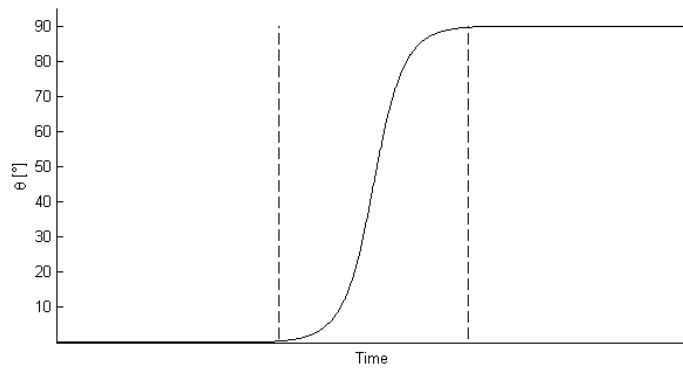
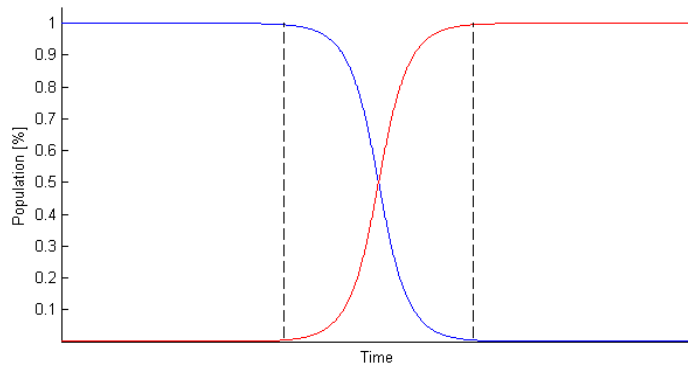
After introducing the eigenstates (Eqs. 2.17) and the eigenvalues (Eqs. 2.18) the transfer process itself will be discussed in more detail.

The objective at hand is to control the state vector $|\psi\rangle$ in order to control the distribution of population among the three states. For the sake of argument the NV⁻ is in the $m_s = -1$ state at the beginning and hence $|\psi\rangle$ is identical to $|-1\rangle$. After the transfer process the NV⁻ should end up in the $m_s = +1$ state, whereby $|\psi\rangle$ is parallel to $|+1\rangle$. However, transient placement of population into $|0\rangle$ has to be avoided.

As $|a^+\rangle$ and $|a^-\rangle$ are linear combinations of all three bare states, which includes $|0\rangle$, population in either one of these dressed states has to be avoided. $|a^0\rangle$, on the contrary, is free of any contribution from $|0\rangle$ and thus is the appropriate tool for transferring population from $|-1\rangle$ to $|+1\rangle$ without populating $|0\rangle$.

By looking at the mixing angle θ (Eq. 2.16) a certain way of doing the transfer process can be found (see Fig. 2.10). θ can be controlled experimentally through the ratio of the Rabi frequencies Ω_{\pm} and should be zero at the beginning, because in this case $|a^0\rangle$ is identical to $|-1\rangle$ as well as $|\psi\rangle$. In order to set θ to 0° , Ω_+ has to have a non-zero value while Ω_- has to be zero. After the increasing Ω_+ reaches its maximum value it is smoothly reduced and Ω_- is increased simultaneously, resulting in a change of the mixing angle θ from 0° to 90° . By doing that $|a^0\rangle$ is rotated into a position parallel to $|+1\rangle$ in a plane perpendicular to $|0\rangle$. Therefore $|a^0\rangle$ never acquires a component of $|0\rangle$ during this motion. If the coupling of the states by the driving field is strong enough and Ω_- and Ω_+ are increased and decreased smoothly, $|\psi\rangle$ (or the flow of population) follows the motion of $|a^0\rangle$ adiabatically. In the end $|\psi\rangle$ is parallel to $|+1\rangle$ and STIRAP is completed.

A loss of population of the trapped state $|a^0\rangle$ may occur due to non-adiabatic transfer to the states $|a^{\pm}\rangle$. Therefore, the condition for adiabatic following is that the non-adiabatic

(a) Rabi frequencies Ω_{\pm} (b) Mixing angle θ 

(c) States

Fig. 2.10: Stimulated Raman adiabatic passage. The NV⁻ starts in $| - 1 \rangle$ and ends in $| + 1 \rangle$. a.) The time evolution of the Rabi frequencies of Ω_- -pulse (blue) and Ω_+ -pulse (red) is shown. Typical for STIRAP measurements the Ω_+ -pulse precedes the Ω_- -pulse. b.) The mixing angle θ is plotted over time. During the STIRAP transfer the mixing angle θ changes from 0° to 90° (see Eqs. 2.16) c.) The time evolution of the NV⁻ state is shown. The initial state is $| - 1 \rangle$ (blue) and due to the STIRAP transfer the NV⁻ reaches its final state $| + 1 \rangle$ (red).

coupling $|\langle a^\pm | \dot{a}^0 \rangle|$ is small compared to the field induced splitting $|\omega^\pm - \omega^0|$ of the energies of these states [28]

$$|\langle a^\pm | \dot{a}^0 \rangle| \ll |\omega^\pm - \omega^0| \quad (2.19)$$

Using Eqs. 2.17 one finds $|\langle a^\pm | \dot{a}^0 \rangle| = \dot{\theta} \sin \phi$ and with $\sin \phi = 1$ Eq. 2.19 can be written as

$$|\dot{\theta}| \ll |\omega^\pm - \omega^0| \quad (2.20)$$

Finally, using Eq. 2.16 it is easy to show that Eq. 2.20 can be written in the form [30]

$$\left| \frac{\dot{\Omega}_- \Omega_+ - \Omega_- \dot{\Omega}_+}{\Omega_-^2 + \Omega_+^2} \right| \ll |\omega^\pm - \omega^0| \quad (2.21)$$

This may be considered to be a 'local' adiabaticity criterion, because both sides can be evaluated at any given time. As long as the condition in Eq. 2.21 is satisfied throughout the interaction non-adiabatic coupling is small. Furthermore, a convenient 'global' adiabaticity criterion can be derived from Eq. 2.20 by taking the time average of the left-hand side $\langle \dot{\theta} \rangle = \frac{\pi}{2\Delta\tau}$, where $\Delta\tau$ is the period during which the pulses overlap, and setting the right-hand side $|\omega^\pm - \omega^0| = \Omega_{eff}$ with $\Omega_{eff} = \sqrt{\Omega_-^2 + \Omega_+^2}$. This leads to

$$\Omega_{eff} \Delta\tau > 10 \quad (2.22)$$

where the numerical value 10 is obtained from experience and numerical simulation studies [28].

At this point it is important to mention that many of the two-tone transitions performed in this thesis are not real STIRAP processes, rather STIRAP-inspired processes. However, the underlying ideas are the same. A major difference is that not only smooth transfer pulses are used, like Gaussian pulses, but also rectangular pulses, which do not fulfil the condition of adiabaticity. Moreover, the counterintuitive pulse sequence described before is often not implemented as there is no delay between the two transfer pulses.

3 Experimental setup

In this chapter I will describe the most important components of the experiment. I will start with the optical setup. Afterwards I will describe the microwave sources and chains used in the experiment in detail.

3.1 Optical setup

The optical setup for this experiment is rather simple, consisting of a confocal microscope with laser excitation and single-photon fluorescence detection (see Fig. 3.1). As the setup was already built at the beginning of this thesis only a short overview outlining the basic ideas will be given - for more details, the reader is referred to Ref. [31].

The light for excitation is provided by a frequency doubled solid state laser (~ 500 mW, 532 nm), which can be stabilized using the first acousto-optic modulator (AOM). An AOM generates a diffraction pattern, where the power of the laser beam of the first and higher orders can be regulated by the AOM. By choosing the first diffraction order with an iris diaphragm, picking off a few percent of the laser beam at the beam sampler and focusing it on a photo diode a feedback loop can be created, which intensity-stabilizes the excitation light from this point forward. The laser beam intensity itself is chosen by the relative positions of the half-wave plate retarder and a polarizer directly after the laser diode ($\perp \dots 0\%$ and $\parallel \dots 100\%$ laser power).

The beam is then focused onto a second AOM, which is optimized for fast switching and therefore used to chop the laser, generating laser pulses with a rise- and fall-time of a few nanoseconds. Furthermore, this AOM controls the excitation light intensity, which is monitored by a second photo diode. By calibrating the photo diode to the actual laser beam power at the objective the excitation light intensity can be chosen.

In order to separate the sensitive beam preparation part from the actual experiment the laser beam is coupled into a single-mode polarization maintaining fibre. Moreover using this fibre cleans up the beam profile as only the lowest order Gaussian beam is transmitted. After the fibre a second half-wave plate retarder is used as each of the four NV⁻-families (see Sec. 2.1) fluoresces most for a specific polarization direction.

A dichroic mirror follows, which reflects the incoming laser beam through the objective onto the NV⁻, but lets the fluorescence light from the NV⁻ pass since the dichroic mirror is transparent for light with a wavelength larger than 658 nm. This fluorescence light is focused onto a pinhole and an additional 650 nm long-wavelength-pass filter, which cuts most of the undesired NV⁰ fluorescence. Finally two avalanche photo diodes (APDs) detect the fluorescence photons and generate pulses, which are registered by a very fast time-to-digital converter card and are uploaded to the control PC.

The objective used in this experiment is a Olympus PLAPON 60XO, which is apochromatic and spring loaded and has an NA of 1.42 and a working distance of 150 μm .

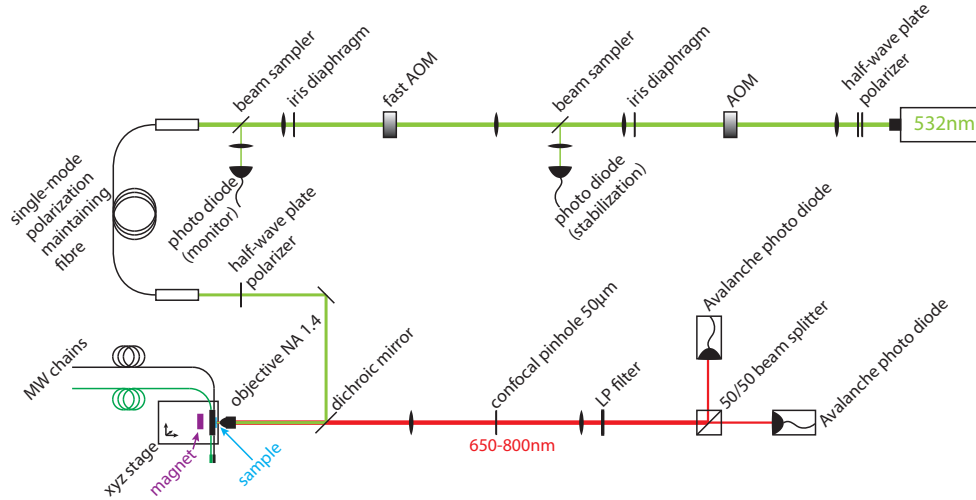


Fig. 3.1: Sketch of the optical setup. The green line is the green laser light, while the red one is the fluorescence light from the NV^- . All components except lenses are labelled in the sketch and the details are explained in the text. Depending on the experiment one (black MW chain) or more (turquoise MW chain) microwave cables are brought to the sample (see Sec. 3.2).

The high numerical aperture is chosen in order to collect as many photons as possible and immersion oil is used to match the refractive index of diamond more closely ($n_{\text{diamond}} = 2.4, n_{\text{oil}} = 1.518, n_{\text{air}} = 1.0$) in order to reduce the angle of total internal reflection between sample and objective.

3.2 Microwave setup

In order to perform spin manipulations, microwave signals (MW) are installed. A range of 2.87 ± 1 GHz is needed as an applied magnetic field shifts the transition frequency $|0\rangle \Rightarrow |-1\rangle$ ($|0\rangle \Rightarrow |+1\rangle$) to roughly 2.07 GHz (3.67 GHz) as nuclear spin polarization is desired [32]. Furthermore fast chopping for pulsed measurements (Sec. 4.1 and Sec. 4.2) as well as pulse shaping (Sec. 4.2.4) is required. Therefore several MW devices are necessary, which will be discussed in the following. A sketch of the MW chain is illustrated in Fig. 3.2.

Firstly, four different MW sources are needed as both transitions has to be driven on and off resonance - more details follow in Sec. 4.2.4. The main carrier signal is provided by a signal generator (Anritsu 3691B) operating with a maximum power output of 17 dBm in a frequency range from 10 MHz to 10 GHz. The output signal is fed into the local oscillator (LO-) input of an IQ mixer (Marki Microwave IQ-1545) mixing two channels of an arbitrary-waveform generator (homemade AWG with an Opal Kelly XEM6010) onto the carrier signal. The AWG is able to generate signals with a temporal resolution of 5 ns and a rise- and fall-time within the same magnitude. The IQ mixer has its optimal working point at 13 dBm, therefore the power of the Anritsu 3691B is chosen accordingly. The second signal is generated by a Thurlby Thandar TGR6000, which operates in a

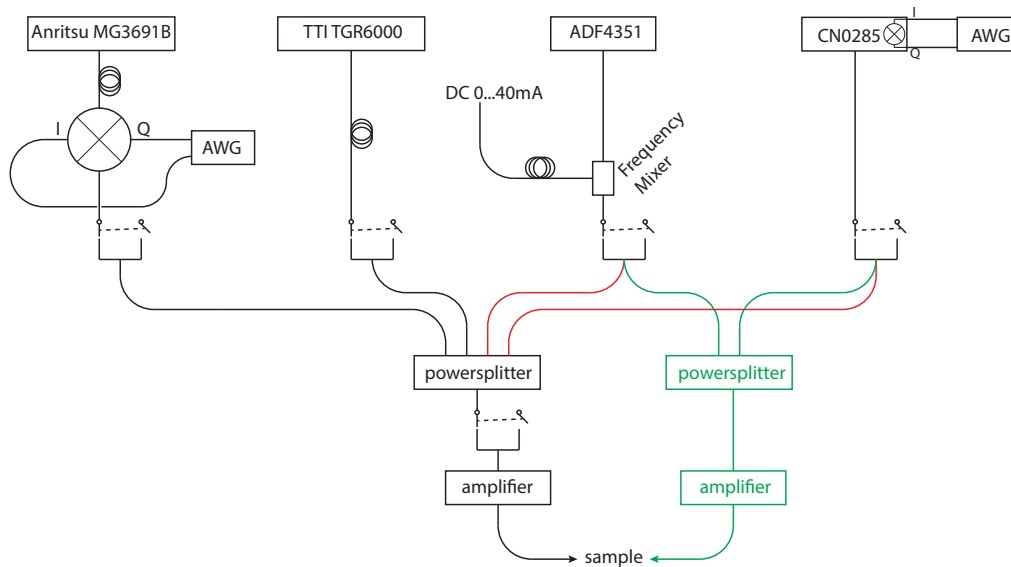


Fig. 3.2: Sketch of the microwave chain. Four sources provide signals in a range of 2.87 ± 1 GHz. Two of the sources (Anritsu MG3691B and CN0285) are paired with arbitrary-waveform generators in order to shape the microwave pulses. A switch for each source allows to choose which signals are sent to the sample. Afterwards the signals are combined according to the conducted experiment (red or green) and amplified by 45 dB.

frequency range from 10 MHz to 6 GHz with a maximum output power of 7 dBm. As this MW source is used for driving the transition resonantly no further manipulating of the signal is required. The final two signals are provided by two wideband synthesizers with integrated voltage controlled oscillator (Analog Devices ADF4351), where one is paired with a wideband transmit modul (Analog Devices ADL5375), which works as an IQ mixer with an optimal working point of 0 dBm (Analog Devices CN0285). Another homemade AWG provides the analog I/Q signals. The ADF4351s generate a signal with a frequency in the range from 35 MHz to 4.4 GHz and an adjustable power (-4 dBm, -1 dBm, 2 dBm or 5 dBm) - -1 dBm is chosen as it fits the working point of the ADL5375 best.

Secondly, switches (Mini-Circuits ZASWA-2-50DR+) are placed after each source to choose between the different signals or more signals simultaneously. From this point on the microwave chain depends on the conducted experiment (red or green coloured parts in Fig. 3.2). On the one hand all four signals are combined in a power splitter (Mini-Circuits ZB4PD-462W+) with a fast switch (Custom Microwave Components CMCS0947A-C4) afterwards, which chops the final signal with a temporal resolution of 3 ns. The RF-signal is then fed into a microwave amplifier (Mini-Circuits ZHL-16W-43+), amplifying the signal by 45 dB (black/red parts in Fig. 3.2) and sent to the sample. On the other hand the two signals of the ADF4351s are combined separately (green) as well as the signals from the Anritsu 3691B and the TGR6000 (black). Each combined signal is fed into a 45 dB-amplifier and sent to the sample individually (black/green parts in Fig. 3.2).

4 Measurement schemes

In this chapter I will give an overview about the fundamental measurement techniques such as ODMR and Rabi oscillations, which are the foundation of every measurement. Afterwards I will go into a little more detail about measuring the different decoherence times described in Sec. 2.4. I will finish this chapter with a description of the sequence needed for the two-tone transfer mentioned in Sec. 2.6.

4.1 Optically detected magnetic resonance

The optically detected magnetic resonance (ODMR) measurement is based on the difference in fluorescence light for $m_s = 0$ and $m_s = \pm 1$ states (see Sec. 2.2.2 and Fig. 2.3) and is the underlying measurement for all following measurements as the frequency for both transitions can be determined. After initializing the NV^- in $|0\rangle$ with a laser pulse via the spin-dependent optical dynamics outlined in Sec. 2.2 and Fig. 2.2, it is transferred to $|\pm 1\rangle$ with a MW signal of constant power. Another laser pulse excites the NV^- and the fluorescence photons are counted in roughly the first 300 ns of the laser duration. The rest of the laser pulse is used to initialize the NV^- again. While continuously transferring, exciting and counting the fluorescence the MW signal is swepted over a frequency range, lasting a few milliseconds at each step. Integrating over many such sweeps may be necessary to detect dips of the fluorescence rate at certain MW frequencies, which correspond to resonant spin transitions (see Fig. 4.1).

In order to resolve the fine and hyperfine structure the MW power has to be lowered as power broadening of the resonance lines is reduced. Furthermore applying a MW- π -pulse instead of a CW MW signal increases the contrast. At last a magnetic field of about ~ 30 mT is applied along the NV axis in order to partially polarize the nuclear spin [32] resulting in an even higher ODMR contrast.

4.2 Pulsed measurements

Using the resonance frequencies obtained from ODMR spectroscopy, pulsed MWs can be applied to coherently manipulate the spin state. As good initialization in $|0\rangle$ is necessary to make spin manipulations of the NV^- controllable, every experimental sequence starts with a $5.5 \mu\text{s}$ laser pulse, which populates the $m_s = 0$ sub-level of the ground state with a high probability via the spin-dependent optical dynamics outlined in Sec. 2.2 and Fig. 2.2. The metastable singlet state has a lifetime of roughly 300 ns, therefore a waiting time of $1.5 \mu\text{s}$ follows, in order to wait for the population to decay to the optical ground state. Afterwards a series of MW pulses is applied, possibly interleaved with waiting times, depending on the experiment carried out. Finally, in order to readout the spin state the laser is switched on again and the fluorescence time traces (see Fig. 2.4) are recorded. This sequence is

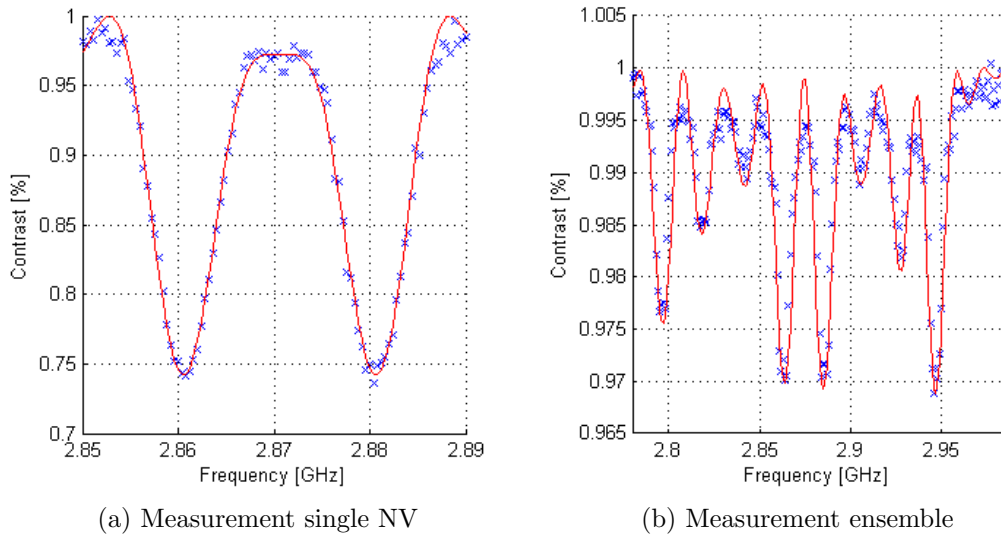


Fig. 4.1: Optically detected magnetic resonance measurement. By sweeping the MW frequency of an applied π -pulse resonance lines of the NV^- can be found depending on the magnetic field. The blue crosses represent the data points and the red line is a fit function a.) ODMR measurement of a single NV^- shows two resonance dips symmetric around 2.87 GHz representing either the transition $|0\rangle \Leftrightarrow |-1\rangle$ or the transition $|0\rangle \Leftrightarrow |+1\rangle$. The MW power is too high to resolve hyperfine structure. The fit consists of two functions according to Eq. 2.14 with a FWHM of ~ 7 MHz. b.) In an ODMR measurement of a NV^- ensemble four resonances per spin state can be found due to the four possible orientations of a NV^- in the diamond lattice. In small magnetic fields the resonances are again symmetric around 2.87 GHz. The fit consists of eight functions according to Eq. 2.14 with a FWHM of ~ 7 MHz.

repeated several million times for each point in the parameter space, which delivers smooth fluorescence traces. The result is then obtained by normalizing the number of counts in the first 200–300 ns of the laser pulse to an equally long counting window 4.5 μs later when the system has reached its equilibrium state. By scanning different parameters in such a measurement different behaviours can be observed, like Rabi nutations or dephasing effects.

4.2.1 Rabi nutations

A MW signal at a certain frequency can transfer the spin state, however, this transfer does not happen instantaneous. The rate of the transfer which depends on amplitude, polarization and detuning of the MW has to be determined. This is done by scanning the length τ of the MW pulse and reading out the spin state (see Fig. 4.2a). The state oscillates between the brighter $|0\rangle$ and darker $|\pm 1\rangle$ state at a given Rabi frequency, as shown in Fig. 4.2b. If the polarization of the MW is not altered and the MW is always driven on resonance, the resulting Rabi frequency only depends on the amplitude and thus

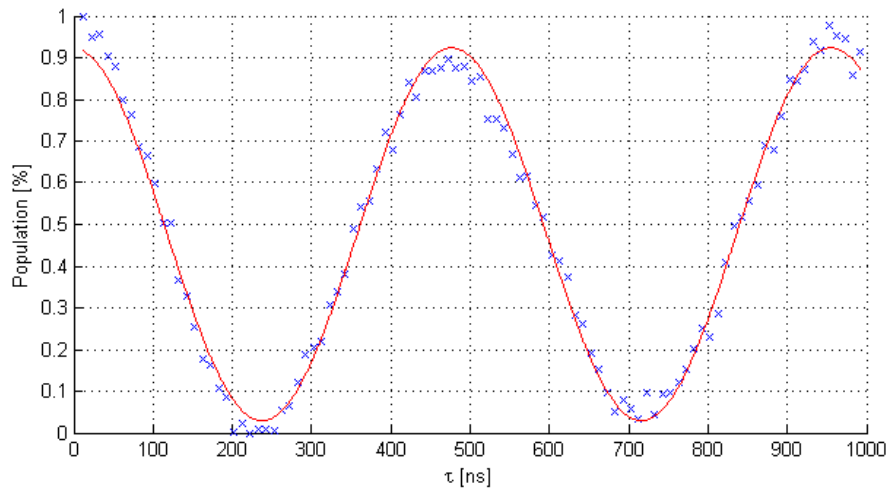
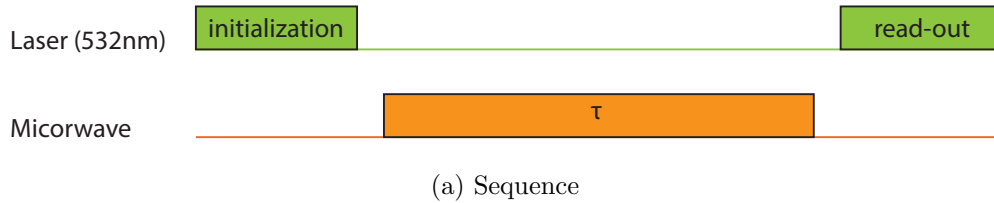


Fig. 4.2: Rabi nutation measurement. a.) The required sequence of laser pulse and MW pulse is sketched. After an initialization pulse of the green laser (green) a MW pulse (orange) with a duration τ is applied. The duration τ is varied and the typical Rabi oscillation is acquired. The read-out pulse works as initialization pulse as well and the sequence is repeated several thousands of times for each duration point. b.) With the described sequence a Rabi oscillation is observed. The frequency depends on the applied MW power and has in this case a value of $2\pi \times 2.17$ MHz. The obtained counts are normalized in a way, that the maximal value represents a fully populated spin ground state and the minimal value an fully populated spin excited state. The blue crosses are the normed data points, while the red curve is a sine fit function.

on the power ($P \propto A^2$). Moreover, the time needed for a π -spin-flip can be determined as well as the duration of the MW to drive the spin into an equal superposition of $|0\rangle$ and $|\pm 1\rangle$ with a $\frac{\pi}{2}$ -pulse. Since dephasing processes, which happen on timescales ranging from tens of nanoseconds in dense ensemble samples to tens of microseconds in pure single-NV samples, limit the maximum duration of coherent manipulation experiments, the transfer has to be driven faster than the dephasing and corresponding high MW amplitudes have to be achieved. With gold micro-structures directly on the sample Rabi frequencies as high as $2\pi \times 7.96$ MHz can be achieved. When using a gold wire above the sample to deliver the MW, values on the order of $2\pi \times 1.59$ MHz are possible.

As shown in Sec. 2.3 the spin resonance transitions are always hyperfine triplets leading to interactions of several detuned spins with the driving field and therefore resulting in beatings of the Rabi oscillations when working with single NV^- . In dense ensemble samples the different frequencies of the spins average out and the beatings are no longer observable.

4.2.2 Free induction decay measurement

In Sec. 2.4 it was already mentioned that T_2^* can be measured with a Ramsey-type (free induction decay - FID) measurement. Before starting the spin manipulation the spin is initialized in $|0\rangle$ with green laser light. Then a $\frac{\pi}{2}$ -pulse follows, which creates an equal superposition $|\psi\rangle = \frac{1}{\sqrt{2}}(|0\rangle + |1\rangle)$ of the two qubit states. By waiting a certain amount of time τ , during which the spin can evolve freely, the two components may pick up a relative phase due to interactions with surrounding magnetic moments (spin bath) or inhomogeneous broadening, which is converted into a population difference by the final $\frac{\pi}{2}$ -pulse and read out optically (see Fig. 4.3a).

Without a spin bath environment the signal would simply oscillate at a frequency corresponding to the MW detuning, because the phase shift is proportional to the free precession time τ and to the detuning δ of the driving field ($\Delta\phi \propto \delta\tau$). However, due to the ^{14}N hyperfine structure, a beating of three oscillations can be observed with frequencies corresponding to three detunings δ , $\delta - 2.2$ MHz and $\delta + 2.2$ MHz. Fortunately, with the help of nuclear spin polarization the beating due to the ^{14}N hyperfine structure can be avoided as one of the NV^- spin states is populated with a high probability [32], while the other two have low population probability.

Furthermore, a decay envelope of the FID signal can be observed, if additional spins from a dephasing bath are present. These spins cause slightly different effective magnetic fields at the location of the NV^- spin resulting in a beating of precession frequencies of the components of the superposition state, which sums up to said decay envelope. The timescale of T_2^* of the decay is given by the mean of the interaction strength with the spins of the bath (see Fig. 4.3). Using an ensemble of NV^- spins instead of a single spin in a dephasing bath, a similar effect occurs: A decay envelope of the FID signal is observed due to the fact that the resonance frequency of each spin of the ensemble is slightly different from the others (inhomogeneous broadening). However, a beating is no longer observed as the large amount of different frequencies average out.

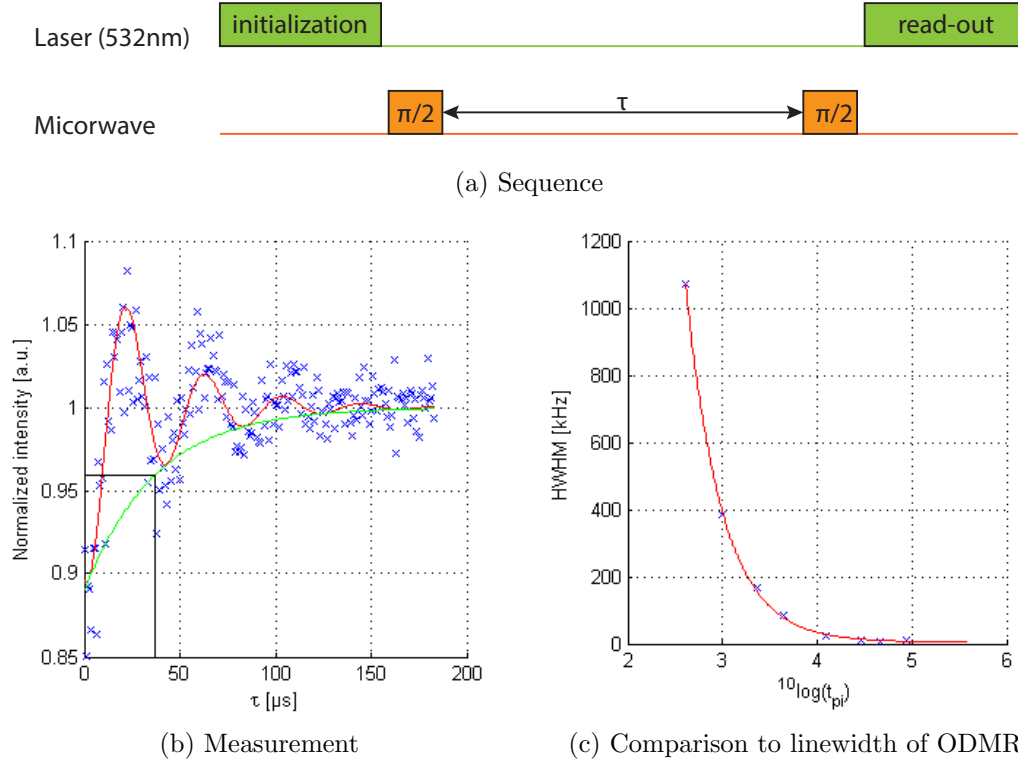


Fig. 4.3: Free induction decay measurement. a.) A sketch of the sequence is shown. After an initialization pulse of green light (green) a MW $\frac{\pi}{2}$ -pulse (orange) rotates the spin vector to the equator of the $|0\rangle \Leftrightarrow |\pm 1\rangle$ -Bloch-sphere. A waiting time of duration τ follows and a second $\frac{\pi}{2}$ -pulse rotates the spin vector further. The duration τ of the waiting time is changed for each measurement point. After a read-out laser pulse the sequence is repeated. b.) Applying the FID sequence with detuned $\frac{\pi}{2}$ -pulses results in an oscillating function of the fluorescence counts with a decay envelope. A detuning of 125 kHz is chosen. The blue crosses are the data points and the red curve is an exponential decaying sine fit function, while the green line is the decay envelope. A dephasing time-constant T_2^* of 33 μs is obtained from a single NV⁻-sample. c.) As mentioned in Sec. 2.4 T_2^* can also be obtained from the FWHM of ODMR measurements. Using Eq. 2.2 T_2^* should be $\sim 23.9 \mu\text{s}$. The difference can be explained from perturbations of the magnetic field, the temperature etc. while doing ODMR measurements resulting in a broader line-width.

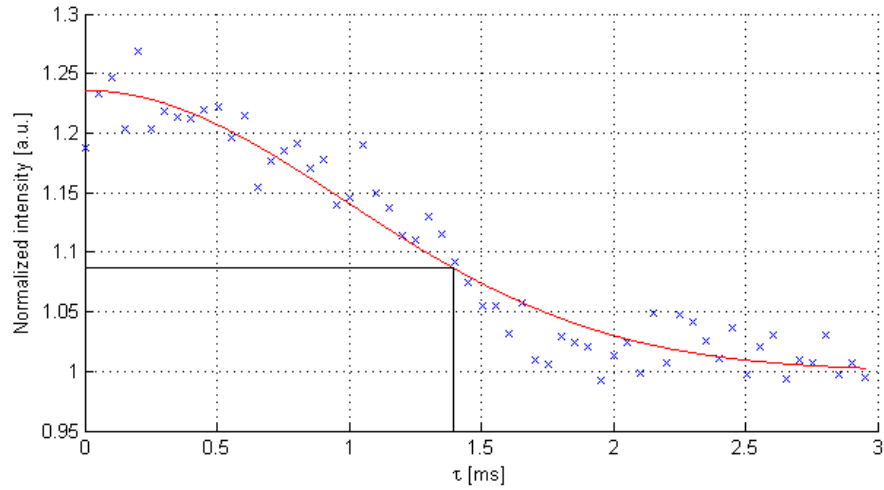
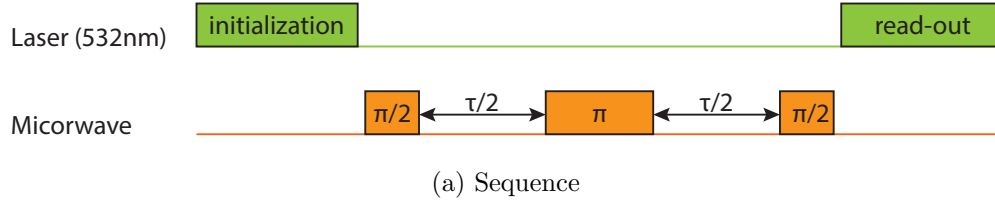


Fig. 4.4: Spin echo measurement. a.) The described sequence is pictured: After an initialization pulse of the green laser (green) the spin vector is rotated with a $\frac{\pi}{2}$ -pulse (orange) to the equator of the $|0\rangle \leftrightarrow |\pm 1\rangle$ -Bloch-sphere. In contrary to the FID sequence a π -pulse (orange) is inserted in between the waiting time τ symmetrically. After the second $\frac{\pi}{2}$ -pulse (orange) a read-out pulse (green) is applied and the sequence is repeated. The total waiting time duration τ is changed for each measurement point although it is halved. b.) Applying the spin echo sequence results in a dephasing time-constant T_2 , which in case of single NV^- samples is larger and has an value of about 1.4 ms. The blue crosses are the data points and the red curve is a Gaussian fit function.

4.2.3 Spin echo measurement

In Sec. 2.4 was stated that T_2^* refers to the timescale of dephasing that is reversible, therefore techniques to recover coherence from the bath can be found. The simplest technique is the spin echo sequence (sometimes called Hahn echo) $\frac{\pi}{2} - \frac{\tau}{2} - \pi - \frac{\tau}{2} - \frac{\pi}{2}$: Differently from FID, where a generated superposition state evolves for a precession time τ and is read out, the precession time τ is cut in half and a π -pulse is inserted in the middle of those equally long precession times $\frac{\tau}{2}$ (see Fig. 4.4a). This additional pulse causes the dephasing of the system spin (the NV^-) to be reverted and the quantum information to be refocused from the bath onto the NV^- -spin, as long as the bath has a coherence time longer than the system. Furthermore all noise components of the bath slower than $\frac{\tau}{2}$ get cancelled out in this symmetrized measurement causing an extended coherence time of the signal known as T_2 .

Usually spin echo signals show collapses and revivals at the Larmor frequency of the ^{13}C nuclear spin due to the limiting surrounding spin bath. If the precession time $\frac{\tau}{2}$ matches the bath precession time, the phase shifts during the de- and rephasing intervals get exactly cancelled out. However, the height of the revival peaks decays on T_2 timescale, since the coherence time of the bath itself is limited.

Normally T_2 is considerably longer than T_2^* and goes up to milliseconds in isotopically purified samples, limited by external magnetic field noise. Considering ensemble samples based on nitrogen-rich raw material the situation changes as the spin bath is dominated by substitutional nitrogen centres. T_2 decreases and is in most cases on the same order of magnitude as T_2^* . Moreover, revivals can no longer be observed since electron spins interact more with each other and the environment than the nuclear spins and hence lose their coherence more quickly.

4.2.4 Two-tone transitions

All of the previous measurements were done in either the $|0\rangle \Leftrightarrow |-1\rangle$ or the $|0\rangle \Leftrightarrow |+1\rangle$ subsystem of the three-level system of the NV^- . Spin manipulations in these two-level systems require only one MW source and can be done quite easily in the experiment. One major characteristic is that the magnetic spin quantum number changes by one ($\Delta m_s = 1$) and are thus single photon processes. However, transitions between $|-1\rangle$ and $|+1\rangle$ are achievable as well, which was discussed in Sec. 2.6. In contrary to $|0\rangle \Leftrightarrow |\pm 1\rangle$ transitions the magnetic spin quantum number changes by two ($\Delta m_s = 2$), which is forbidden in one-photon transitions, implying that two-photon processes have to take place requiring at least two MW sources.

One of the advantages of using the $|-1\rangle \Leftrightarrow |+1\rangle$ subsystem is that the population transfer is more robust against small variations of experimental conditions like MW stability, pulse timing and pulse shape. Moreover, in case of single NV^- T_2^* of the $|-1\rangle \Leftrightarrow |+1\rangle$ subsystem tends to be larger than T_2^* of the $|0\rangle \Leftrightarrow |\pm 1\rangle$ subsystem, which improves many measurements in terms of decoherence. In this experiment, however, the biggest advantage is that two MW signals are required in order to complete a population transfer. The two signals can be applied via two separate wires (e.g. crossed wires) and a transfer can only happen if the transfer conditions are correct regarding both MW signals at the location of the NV^- . A more detailed discussion will follow in Ch. 5.

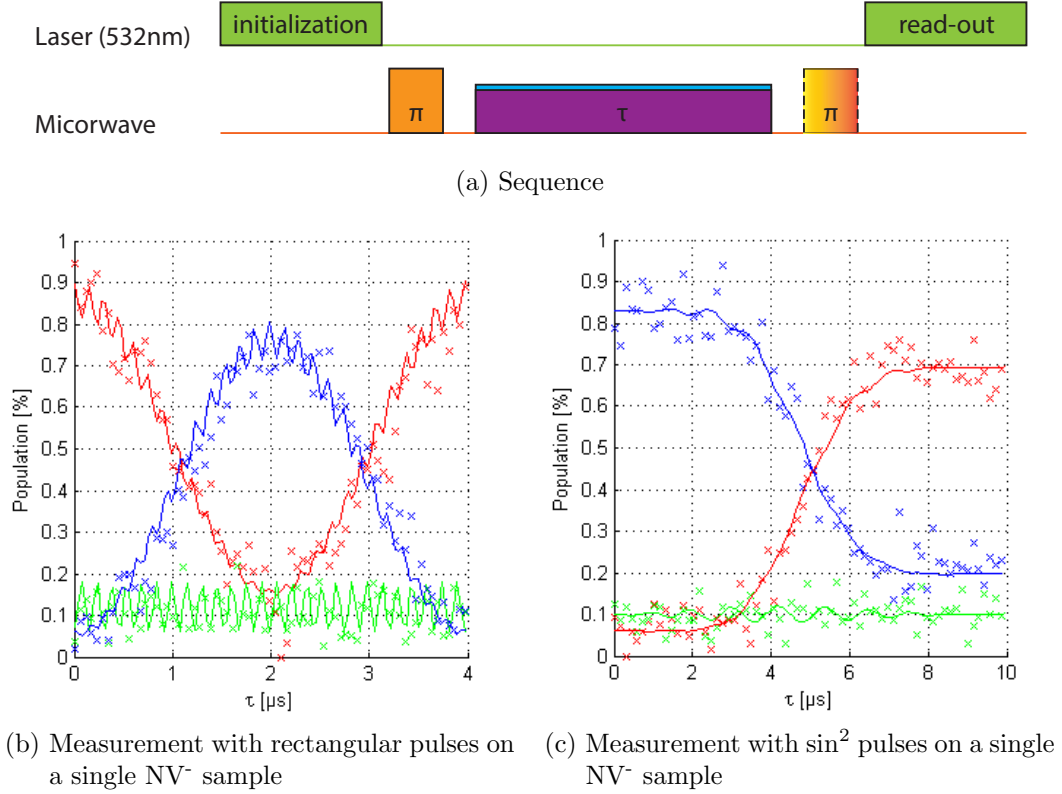


Fig. 4.5: Two-tone transition measurement. a.) The sequence starts with an initializing pulse of green laser (green) and is followed by a resonant π pulse (orange) of one of the four MW sources. Afterwards the two-tone pulses (violet and blue) driven by two other MW sources are applied for a changing duration τ . Before reading out the state optically (green) either a π -pulse resonant to $|0\rangle \Leftrightarrow |\pm 1\rangle$ or no π -pulse at all (dashed yellow/orange) is applied depending on the interested NV^- spin state. b.)+c.) The NV^- gets initialized in $|-1\rangle$ (blue) with the first resonant $\frac{\pi}{2}$ -pulse. Due to a detuning of the two-tone pulses $|0\rangle$ (green) does not get populated during the whole transition time. Crosses are data point, while the curves are fit functions. b.) Applying the rectangular two-tone pulses results in a transfer to $|+1\rangle$ (red). As the two-tone pulses are not switched off after a successful transfer the population starts moving back to $|-1\rangle$ resulting in an oscillation between $|-1\rangle \Leftrightarrow |+1\rangle$. The fit functions are determined by solving the Hamiltonian (Eq. 2.15) for each spin state with initial conditions of imperfect electron spin polarization and rectangular two-tone pulses and evolve the solution in time. c.) Applying the \sin^2 two-tone pulses results in a transfer to $|+1\rangle$ (red). In contrary to rectangular pulses the population of the NV^- stays the same after the transfer, although the power of the two-tone pulses is not yet zero. The fit functions are determined by solving the Hamiltonian (Eq. 2.15) for each spin state with initial conditions of imperfect electron spin polarization and \sin^2 two-tone pulses and evolve the solution in time.

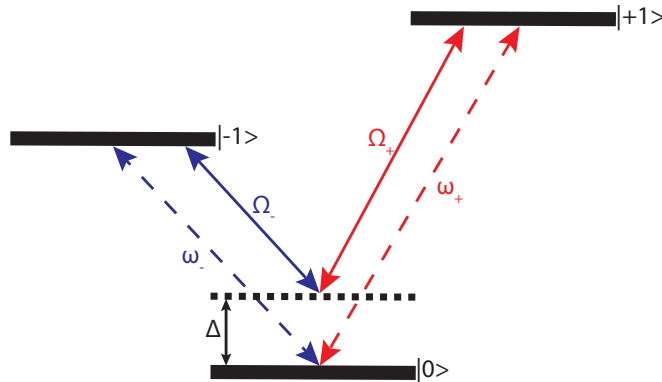


Fig. 4.6: Required MW transitions in order to perform two-tone transfer. Blue lines drive the transition $|0\rangle \leftrightarrow |-1\rangle$, while red lines drive $|0\rangle \leftrightarrow |+1\rangle$. The dashed blue line is the resonant driving field ω_- and the dashed red line the resonant driving field ω_+ . The two-tone pulses are driven by the fields Ω_- (blue) and Ω_+ (red) with a detuning Δ .

As mentioned before at least two MW sources are required, however in order to implement the two-tone measurement sequence to this experiment four MW sources are needed as on the one hand the state of the NV^- has to be prepared/read out and on the other hand the two-tone transition has to be driven (see Fig. 4.6). The sequence starts with one MW source transferring the population of $|0\rangle$, which has been initialized with a green laser pulse, to $|+1\rangle$ with a resonant π -pulse (ω_+). Afterwards two MW sources drive the detuned two-tone pulses (Ω_+ and Ω_-), which transfer the population to $|-1\rangle$ in a certain time τ . After completion of the transfer, the population of the target state is determined by transferring the population of $|-1\rangle$ by another resonant π -pulse (ω_-) back to $|0\rangle$ where a laser pulse excites the NV^- and the fluorescence photons are counted. $|0\rangle$ and $|+1\rangle$ can be read out as well by applying either no π -pulse at all or a π -pulse (ω_+) resonant to the $|0\rangle \leftrightarrow |+1\rangle$ transition after the two-tone transfer, respectively. Of course, the two-tone transfer can be started from $|-1\rangle$ as well - one only has to swap $|+1\rangle$ and $|-1\rangle$ in the previous text. The sketch of the sequence is shown in Fig. 4.5a.

A detuning is introduced in order to prevent populating $|0\rangle$ during the transfer process as an effective two-level system $|-1\rangle \leftrightarrow |+1\rangle$ is desired. As already mentioned in Sec. 2.6 the condition $\Delta_+ = \Delta_- = \Delta$ has to hold for the whole transfer time. Additionally the MW power of both pulses needs to be the same ($\Omega_+ = \Omega_-$). The pulses used in this experiment are mostly \sin^2 - or rectangular pulses, although arbitrary pulses can be created with the AWGs described in Sec. 3.2. π -pulses for initialization and read-out are always rectangular, while two-tone pulses can be both. Smooth pulses, like \sin^2 -pulses, have the advantage that they come more closely to the adiabatic transfer ideal of STIRAP, whereas rectangular pulses complete the transfer faster at the same maximal MW power and detuning and are generally easier to handle. In case of smooth transfer pulses a certain MW power requires a specific set of parameters, which include the detuning, the width of the pulse and a delay between both pulses. With every parameter set the population transfer needs a certain amount of time to be completed. Rectangular pulses only depend

on the MW power and the detuning. At fixed MW power the transfer needs a longer time to be finished with increasing detuning.

Fig. 4.5 shows a scan of the duration τ of the population transfer for rectangular and \sin^2 pulses, where all three states are read out successively.

5 Matrix control of qubits

Control over individual qubit in large-scale quantum systems is a requirement for many quantum technologies. In case of a two-dimensional array of magnetic spin qubits the difficulty consists in accessing each qubit with control lines, limiting the possibility to scale the quantum system. A method which promises scalable control of NV^- spins with two-tone transitions is tested in the following chapter.

Two-tone transfers, described in Sec. 2.6 and Sec. 4.2.4, require that the two Rabi frequencies (Ω_{\pm}) of the two-tone pulses are of equal magnitude. This requirement can be used to control three-level systems in a grid by applying the two driving fields through crossed wire arrays (see Fig. 5.1b). At a junction of two wires, which transport the fields for either Ω_+ or Ω_- , a NV^- on the surface in a distance r to the wire experiences a Rabi frequency of $\Omega_{\pm} = \eta \frac{\sqrt{P_{MW}}}{r}$, where η is the driving efficiency and P_{MW} is the MW power. By increasing the distance r to the wire the Rabi frequencies Ω_{\pm} decrease, respectively, and therefore the population transfer efficiency gets smaller rapidly. The advantage of two-tone transfer is, hence, that a transfer of the population close to a wire crossing does not affect NV^- s at other sites. Moreover, a large common detuning Δ , which is required to reduce the three-level system to an effective two-level system, can be used to prevent population transfers on the transitions $|0\rangle \Leftrightarrow |\pm 1\rangle$.

Throughout this chapter I will compare single NV measurements with the measurements done with the chip in order to verify the functionality of the chip. Considering the functionality of the chip one has to consider several sources of errors, such as:

- Initializing the NV^- with green laser light is not a process which transfers the state to $|0\rangle$ with a 100 % success rate as already mentioned in Sec. 2.2.2.
- A π -pulse, which swaps the population of two spin states, e.g. $|0\rangle \Leftrightarrow |-1\rangle$, is normally not a process with a 100 % efficiency due to the hyperfine population distribution of the NV^- .
- Relaxation and decoherence mechanisms have to be considered as these mechanisms limit the duration of a measurement sequence.
- The success rate of the transfer $|-1\rangle \Leftrightarrow |+1\rangle$ might not reach 100 % at the intended site. Conversely, a partial two-tone transfer could take place at another crossing as well.
- State $|0\rangle$ of the NV^- should not be populated during the whole two-tone transfer process. Additionally, the initialized state at other crossings should not change due to two-tone transfer pulses, especially along the wire where the MW is applied.

For single NV measurements I use a single-crystal artificial diamond created by chemical vapour deposition (CVD). An epitaxially grown layer of 50 μm thick, isotopically purified

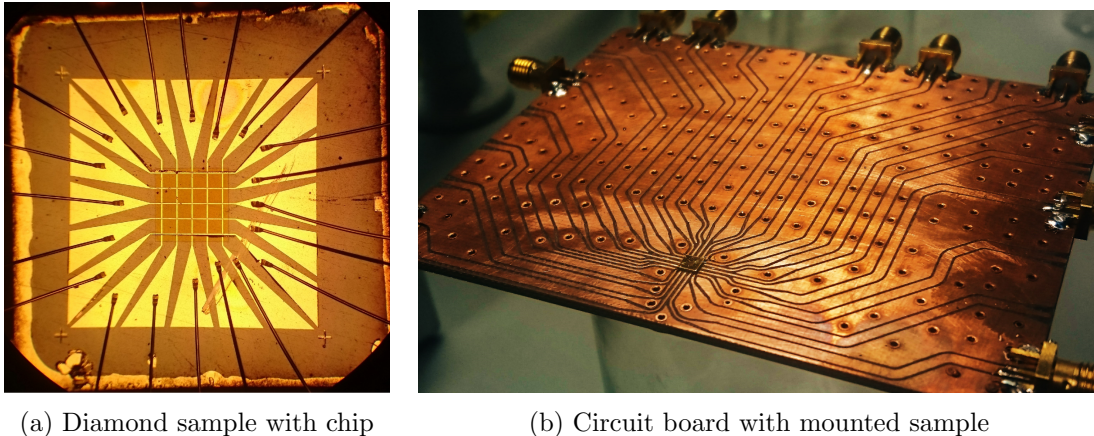


Fig. 5.1: Wire grid chip mounted on a PCB board. a.) The gold structure of the chip is bright yellow. The fine lines in the center are the wire grid, while the rather large area are the connection pads for the bonds. The bonds themselves are the black lines going to each pad. The SiO_2 -layer is hardly visible. b.) The circuit board consists of twenty supply lines, which are designed to have an impedance of $50\ \Omega$. The wholes in the board connect the top ground layer with the bottom ground layer. The diamond sample sits, where all lines come together. SMA connectors are put at the end of the supply lines to connect the board with the diverse MW sources.

to 99.999% ^{12}C hosts the single NV^- centres. The MW fields are applied through a $100\ \mu\text{m}$ gold wire spanned over the diamond surface. For chip measurements, however, I use a NV ensemble, which is hosted by an untreated CVD diamond with natural isotopic abundance and a nitrogen content below 1 ppm. The MW fields are applied through a crossed-wire control grid, described in Sec 5.1.

5.1 Design and production of chip

As the grid is produced directly on the diamond sample, the sample size itself is a limitation for the chip size. The diamond samples used in this thesis have a width and length of about 3 mm and thus the chip cannot be larger than that. In fact it has to be smaller as a gap of about $500\ \mu\text{m}$ to the edge of the diamond is required in order to remove the edge bead, which is a result of the production process. The total size of the grid circuit therefore is $2\ \text{mm} \times 2\ \text{mm}$ and the chip is shown in Fig. 5.1a.

The centre piece of the chip is a wire grid. It consists of 5×5 wires in two layers resulting in 25 crossings. The wires have a length of about $700\ \mu\text{m}$ and a width of $10\ \mu\text{m}$. The height of the wires is different for the two layers. The bottom ones are about $200\ \text{nm}$ thick and the top ones about $400\ \text{nm}$. The distance between the wires in each layer is $125\ \mu\text{m}$ and the layers themselves are separated by $300\ \text{nm}$ SiO_2 . In order to connect the chip with a circuit board, the wires end in pads, which provide a larger area for bonding. The pads are triangular shaped and positioned in a way so they fill the remaining area of the chip in order to be as large as possible. The side closest to the chip edge has a length

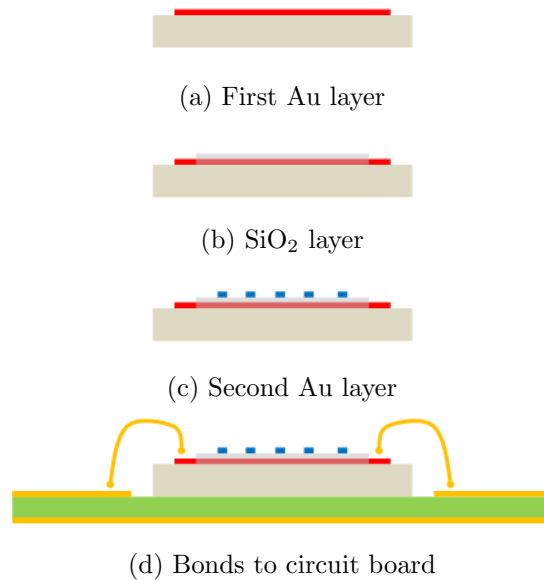


Fig. 5.2: Production steps of wire grid chip. a.) After spray-coating a layer of photoresist onto the diamond and structuring it with lithography a layer of gold is deposited on the diamond (red). b.) A square SiO_2 layer is put on the first Au layer in order to provide insulation between the two gold structures (grey). c.) A second gold layer is deposited on the SiO_2 layer to fabricate a second (orthogonal) wire array (blue) using the same structuring technique. d.) Lastly the wire grid chip is mounted on the circuit board (green) and the connections are established with gold bonds (yellow).

of $350\ \mu\text{m}$ and the minimum distance between two pads is $50\ \mu\text{m}$.

The chip undergoes several steps of depositing and lifting off material to fabricate the required wire grid. Starting the procedure a photoresist, which is a light-sensitive material, is spray-coated onto the diamond. Afterwards the photoresist is structured using optical lithography as it becomes either soluble or insoluble when exposed to light. A thin layer ($10\ \text{nm}$) of titanium together with a $200\ \text{nm}$ thick gold layer are deposited on top of the light-treated photoresist. Then the soluble parts of photoresist are lift off generating the desired pattern (see Fig. 5.2a). A square SiO_2 layer with a thickness of $300\ \text{nm}$ is then applied to provide insulation between the two wire arrays and is structured using the same method (see Fig. 5.2b). Afterwards a second titanium layer ($10\ \text{nm}$) and a second gold layer ($400\ \text{nm}$) is deposited to fabricate the second (orthogonal) wire array with the same procedure (see Fig. 5.2c).

The sample itself is placed on a FR-4 circuit board, which is shown in Fig. 5.1b. The board has a length of $10\ \text{cm}$ and a width of $8\ \text{cm}$ and is $1.55\ \text{mm}$ thick. On the top as well as on the bottom side is a $18\ \mu\text{m}$ thick layer of copper, where the bottom layer serves as ground plane only. On the top layer the wires leading from the SMA connectors to the sample are designed to have an impedance of $50\ \Omega$ at $2.87\ \text{GHz}$ MW frequency, resulting in a width of $1.6\ \text{mm}$ with a $300\ \mu\text{m}$ gap to the surrounding ground planes. The chip is

connected via bonds to the circuit board (see Fig. 5.2d).

5.2 Single NV

As measurements with the wire grid chip have not been done before, the errors listed in the introduction of this chapter are discussed with the help of a single NV⁻ and a single gold wire spanned over the diamond surface first. The reason doing single wire measurements first is that these kind of measurements are well understood and have been done before opposed to the wire grid measurements. However, many qualitatively equal measurements can be performed with a single wire and comparable data can be collected.

The following discussion addresses each error listed in the introduction of this chapter successively concerning single NV⁻s, but with regard to the wire grid chip, especially the success rate of the transitions $| - 1 \rangle \Leftrightarrow | + 1 \rangle$ and $| 0 \rangle \Leftrightarrow | \pm 1 \rangle$.

The errors due to bad initialization of the green laser are not fully experimentally controllable, as the initialization is determined by the transition probabilities between the NV⁻ states (see Fig. 2.2). At high enough laser power, so that the NV⁻ is saturated, the probability to end in the spin ground state $| 0 \rangle$ after several optical cycles is around 80 % (average quoted spin-polarisation from the vast range of spin-polarisations reported [11]). A 100 % success rate is not achievable by simply radiating green light onto the NV⁻. This inconvenience, however, can be regarded for in the analysis of the data. The NV⁻ has to be in one of the three possible spin states ($| 0 \rangle$, $| - 1 \rangle$ or $| + 1 \rangle$):

$$p_{|0\rangle} + p_{|-1\rangle} + p_{|+1\rangle} = 1 \quad (5.1)$$

where $p_{|0\rangle}$, $p_{|-1\rangle}$ and $p_{|+1\rangle}$ are the population probabilities, respectively. Additionally, the real photon counts c for each state can be expressed by

$$\begin{aligned} c_{|0\rangle} &= p_{|0\rangle} \Delta c + c_{min} \\ c_{|-1\rangle} &= p_{|-1\rangle} \Delta c + c_{min} \\ c_{|+1\rangle} &= p_{|+1\rangle} \Delta c + c_{min} \end{aligned} \quad (5.2)$$

with c_{min} being the theoretically minimal photon counts, i.e. fluorescence, if the read-out state is not populated at all, and Δc being the count difference between theoretically maximal and minimal photon counts. As Eq. 5.1 and Eqs. 5.2 create a system of four equations with five unknown variables the system remains analytically unsolvable. An assumption about the probability distribution between the spin states has to be made. Two rather naive ways to make the additional assumption is by assuming either that the minimal real count value is also c_{min} or the initialized state is populated with a probability of 80 %. With that the system of equations (Eq. 5.1 and Eqs. 5.2) is solvable and c_{min} and Δc can be estimated. By having an estimation for c_{min} and Δc the probabilities to find the NV⁻ in a certain spin state at each time step of the two-tone transfer process can be calculated from the data.

Thus, the error due to initialization with green laser light is known and can be accounted for. However, the initialization probability of the green laser is not fully experimentally controllable, i.e. a certain value of initialization probability cannot be exceeded. For the rest of the thesis this will be held in mind, but will not be mentioned explicitly.

After initializing the NV⁻ in $|0\rangle$, spin state manipulations are done, but the success rate of these transfer processes is generally not 100 %. Due to the hyperfine splitting of the NV⁻ (see Fig. 2.6) a transfer pulse is resonant to only one of the nuclear spin states, strictly speaking, and therefore only one third of the population of $|0\rangle$ is transferred, assuming the population probability is the same for all three nuclear spin states. However, a transfer pulse has a certain broadening in the frequency spectrum due to its power and also transfers the population of the other two nuclear spin states partially. By increasing the MW power the probability to transfer the population from $|0\rangle$ gets closer to 100 %. For example, a 100 ns long π -pulse corresponding to a Rabi frequency of $2\pi \times 5.00$ MHz resonant with the $m_I = 0$ hyperfine state of $|-1\rangle$ transfers the population from $|0\rangle$ to $|-1\rangle$ with a probability of $\sim 90\%$. Unfortunately, due to limitations of the MW source output powers and the MW amplifiers shorter π -pulses than 50 ns are not possible with this setup.

Another approach to increase the transfer probability of a π -pulse is to polarize the nuclear spin of the ^{14}N atom [32]. Polarizing the nuclear spin means that the probability to find the NV⁻ in one of the three hyperfine states is increased, while the probabilities for the other two is decreased and ideally goes towards zero. In order to polarize the nuclear spin a magnetic field has to be applied. However, not only the strength of the magnetic field but also its direction is important to polarize the nuclear spin to a high degree. In order to achieve large nuclear spin polarization magnetic fields of several tens of mT have to be applied [32]. Furthermore, the angle between NV⁻-axis and magnetic field vector has to be less than 1° in order to get more than 50 % nuclear spin polarization probability [33]. With a magnetic field strength of 44 mT and a perfectly aligned magnetic field vector a nuclear spin polarization of $\sim 95\%$ is achievable [33].

However, in this experiment the limitation of magnetic field strength arises due to the limitation of the MW frequency of the MW components. The energy splitting due to the Zeeman effect depends on the magnetic field 28 MHz/mT and as most MW components work between 2 GHz and 4 GHz the magnetic field strength is limited to ~ 30 mT with this setup. With a magnetic field strength of 30 mT and a perfectly aligned magnetic field vector a nuclear spin polarization of $\sim 85\%$ is achievable [32]. In Fig. 5.3 a magnetic field of 28.2 mT is applied along the NV⁻-axis and a nuclear polarization of 78.1 % is achieved.

Relaxation and decoherence mechanisms limit the duration of a measurement sequence. After a certain amount of time the spin state of the NV⁻ is not well defined and therefore spin manipulations are not correctly done anymore. The time constants for relaxation and decoherence mechanisms have already been described in Sec. 2.4. In case of single NV centres at room temperature T_1 has a duration of several ms, whereas T_2 is several hundreds of μs long. The smallest time constant is T_2^* , which still has a duration of several tens of μs . Fortunately, a MW pulse used in the two-tone transfer sequence lasts only from ~ 50 ns to maximal a couple of μs . Therefore the errors due to relaxation and decoherence mechanisms can be easily avoided by pulse durations smaller than T_2^* . The longest two-tone pulse lasts around 10 μs .

After explaining errors, which also need to be considered in most other measurement schemes, errors concerning two-tone transitions, which will arise from using the wire grid chip, are discussed. On the one hand two-tone transitions may occur elsewhere than at the intended site. Therefore, the transfer probability depending on the distance to the intended transfer site is determined. Moreover, if not a two-tone transfer some other

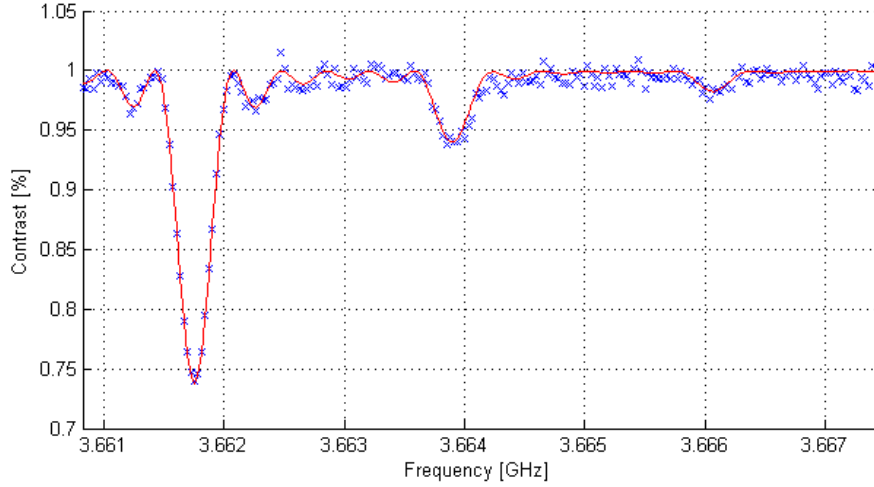


Fig. 5.3: ODMR of a single NV^- with polarized nuclear spin. Scanning the MW frequency of an applied π -pulse with a power corresponding to a Rabi frequency of $2\pi \times 183$ kHz results in a spectrum with three resonance dips fitting the hyperfine transitions. The blue crosses are data points and the red curve is a fit function consisting of three functions according to Eq. 2.14 with a FWHM of ~ 320 kHz. A magnetic field of 28.2 mT is applied and by aligning the field vector with the NV^- -axis a nuclear spin polarization of 78.1 % is achieved.

transitions may occur elsewhere in the wire grid, e.g. $|0\rangle \Leftrightarrow | + 1\rangle$ transitions, which has to be investigated. On the other hand the two-tone transfer itself might not perform as intended, e.g. populating $|0\rangle$ during the process.

As the final goal is to transfer the NV^- state from $| + 1\rangle$ to $| - 1\rangle$ (or vice versa) at a certain crossing of the wire grid and only at that crossing, the effect of the two-tone signals depending on the distance to the crossing is of great interest. In case of single NV^- samples changing the location of the NV^- is impossible, and looking for NV^- s which sit at different distance relative to the wire is a time-consuming process, if there are even NV^- s at this certain distance in the sample. However, the power of the applied MW signals at the site of the NV^- depends strongly on the distance to the wire. Therefore measuring the transfer probability by sweeping the MW power of the two-tone pulses corresponds to a measurement where the location of the NV^- is changed with respect to the wire.

In Fig. 5.4 a MW power sweep of one of the two-tone pulses is shown. The NV^- is prepared in $| + 1\rangle$ by applying a resonant π -pulse after the initialization with green laser light. Afterwards the two-tone pulses are applied in order to transfer the NV^- from $| + 1\rangle$ to $| - 1\rangle$. Lastly the state of the NV^- is readout either by driving a π -pulse resonant to $| - 1\rangle$ or $| + 1\rangle$ or by applying no MW at all. The MW power of the two-tone pulse corresponding to the $|0\rangle \Leftrightarrow | - 1\rangle$ (Ω_-) transition is changed while the power of the other two-tone pulse (Ω_+) is held constant. Thinking of the wire grid this measurement is equal to one, where the distance between NV^- and the wire, which guides the MW corresponding to the $|0\rangle \Leftrightarrow | - 1\rangle$ transition, changes. The measurement in Fig. 5.4 is done with a MW power corresponding to a Rabi frequency of $2\pi \times 2.11$ MHz in the resonant $|0\rangle \Leftrightarrow | \pm 1\rangle$

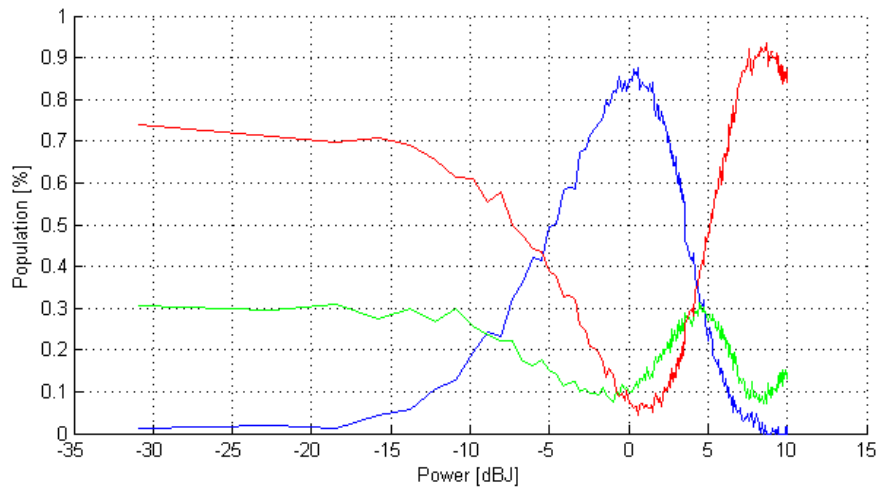


Fig. 5.4: Power scan of one of the two-tone pulses performed with a single NV⁻. The NV⁻ is prepared in $|+1\rangle$ and a two-tone transfer is performed with a MW power corresponding to a Rabi frequency of $2\pi \times 2.11$ MHz and a detuning of 0 MHz. While the power of the Ω_+ -pulse is held constant, the power of the Ω_- -pulse is varied. 0 dBJ is set, where the power of the Ω_+ - and Ω_- -pulse has the same value. The red curve corresponds to population in $|+1\rangle$, the green one in $|0\rangle$ and the blue one in $|-1\rangle$.

transition and with zero detuning. Furthermore, the two-tone pulses are square-shaped and their duration is chosen so that the best transfer success rate is achieved for the chosen MW power ($\tau = 413$ ns). The power scale is determined by

$$p(\text{dBJ}) = 10 \log_{10} \left(\frac{p}{p_0} \right) \quad (5.3)$$

where p_0 is the point, at which both two-tone pulses have the same power, and p is the set power of the Ω_- -pulse. The three different colors in Fig. 5.4 represent the three different spin states of the NV⁻: blue $\leftrightarrow |-1\rangle$, green $\leftrightarrow |0\rangle$ and red $\leftrightarrow |+1\rangle$. The transfer efficiency is largest, as intended, at 0 dBJ, where the MW powers of the two-tone pulses are the same - the population probability of $|-1\rangle$ reaches its maximal value. For decreasing MW power of the Ω_- -pulse the transfer efficiency decreases as well. $|-1\rangle$ gets less and less populated through the two-tone pulses. As reducing the MW power at a fixed distance to the wire is qualitatively equal to increasing the distance to the wire at fixed MW power, the assumption can be made, that in case of the wire grid the two-tone transfer efficiency at a neighbouring crossing is close to zero. Although the population transfer efficiency from $|+1\rangle$ to $|-1\rangle$ is reduced at low MW power of the Ω_- -pulse, a population transfer still occurs in the $|0\rangle \leftrightarrow |+1\rangle$ manifold of the spin states. As the MW power of the Ω_+ -pulse remains the same while the Ω_- -pulse power decreases the two-tone pulses get reduced to simple $|0\rangle \leftrightarrow |+1\rangle$ -transfer pulses. The measurement pulse train therefore resembles one done in Rabi oscillation measurements. Thinking about the wire grid, NV⁻s along the wire carrying the Ω_+ -pulses and at sites at a great distance to the Ω_- -pulse-wire

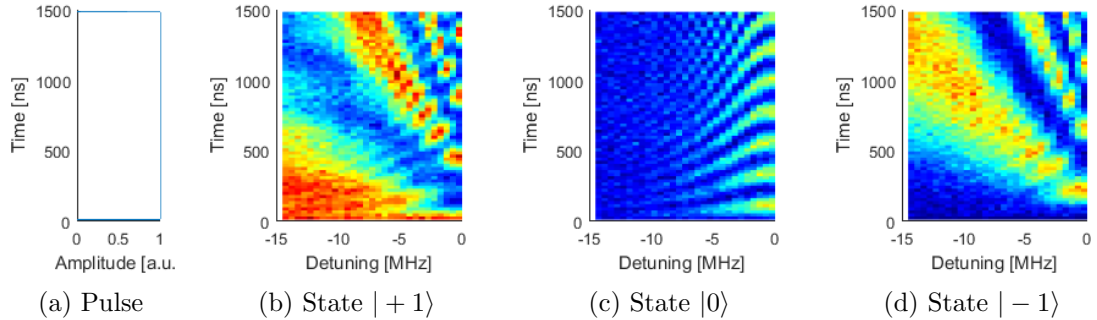


Fig. 5.5: Detuning scan of rectangular two-tone pulses performed with a single NV^- . a.) The pulse shape of the two-tone pulses is pictured. The amplitude is normalized to its maximum value. In this series of measurements the shape of the two-tone pulses is rectangular. b.)-d.) The time trace of each NV^- state (b.) $\rightarrow | + 1 \rangle$, c.) $\rightarrow | 0 \rangle$ and d.) $\rightarrow | - 1 \rangle$) is plotted over the detuning of the two-tone pulses, which have a MW power corresponding to a Rabi frequency of $2\pi \times 3.65$ MHz. The color scale goes from blue (empty state) to red (occupied state).

are simply performing Rabi oscillations between $|0\rangle$ and $|+1\rangle$. However, even transitions in this subspace of the spin manifold of the NV^- are unwanted and therefore a detuning has to be introduced.

The main purpose of using MW signals detuned from the resonance frequency is to reduce the three-level system ($|0\rangle, |-1\rangle, |+1\rangle$) to an effective two-level system ($|-1\rangle, |+1\rangle$) as described in Sec. 2.6, i.e. no population should be in $|0\rangle$ at any given time during the process.

In Fig. 5.5 a detuning scan for rectangular two-tone transfer pulses is shown. The Rabi frequency for the resonant $|0\rangle \leftrightarrow |\pm 1\rangle$ transitions is $2\pi \times 3.65$ MHz. The detuning is plotted on the x-axis, while the y-axis represents the duration of the applied two-tone pulses. The colour shows the population of the state, where red means that the whole population is in that state whereby dark blue stands for an empty state. The two-tone transfer process starts always in $|+1\rangle$, which can be seen in Fig. 5.5b. For small detuning $|0\rangle$ gets partially populated several times during the transfer process (see Fig. 5.5c) and always as transfer state between $|\pm 1\rangle$. By increasing the detuning, $|0\rangle$ becomes less and less populated, whereas the two-tone transfer process is not affected apart from the time needed to complete the transfer. For larger detuning the two-tone pulses have to be applied longer in order to transfer the population from $|+1\rangle$ to $|-1\rangle$ successfully (see Fig. 5.5d).

With a MW power corresponding to a Rabi frequency of $2\pi \times 3.65$ MHz an absolute detuning of at least 13 MHz is needed to significantly suppress the population of $|0\rangle$.

In Fig. 5.6 \sin^2 -pulses are used instead of square pulses. The MW power of the resonant $|0\rangle \leftrightarrow |\pm 1\rangle$ transitions is still the same as for square pulses resulting in a Rabi frequency of $2\pi \times 3.65$ MHz.

The advantages of using \sin^2 -pulses instead of rectangular ones is that \sin^2 -pulses change the MW amplitude very smoothly and come close to the adiabatic following condition mentioned in Sec. 2.6. Moreover, \sin^2 -pulses always start from zero amplitude while

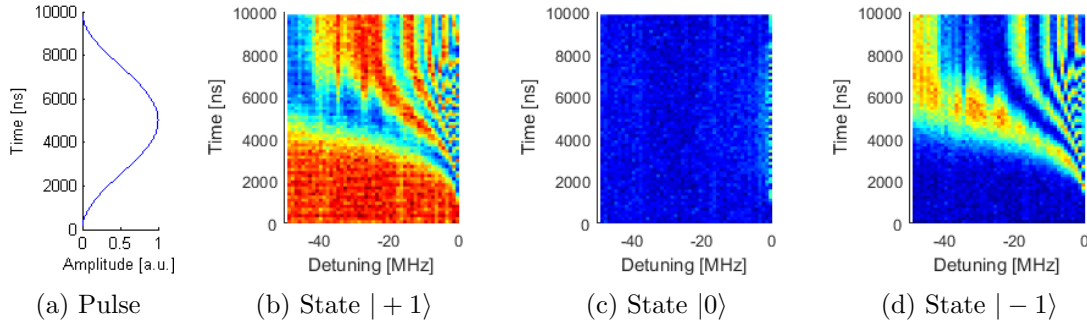


Fig. 5.6: Detuning scan of \sin^2 two-tone pulses performed with a single NV⁻. a.) The pulse shape of the two-tone pulses is pictured. The amplitude is normalized to its maximum value. In this series of measurements the shape of the two-tone pulses is \sin^2 . b.)-d.) The time trace of each NV⁻ state (b.) $\rightarrow |+1\rangle$, c.) $\rightarrow |0\rangle$ and d.) $\rightarrow |-1\rangle$) is plotted over the detuning of the two-tone pulses, which have a maximal MW power corresponding to a Rabi frequency of $2\pi \times 3.65$ MHz. The color scale goes from blue (empty state) to red (occupied state).

Gaussian pulses theoretical only approach zero amplitude. However, as the amplitude is smoothly increased and decreased the time needed to complete the transfer increases which has been explained in Sec. 4.2.4.

A similar behaviour in case of small detuning is observed but not as prominent as for square pulses, i.e. $|0\rangle$ gets populated only close to resonance. Starting from a detuning of about 5 MHz, $|0\rangle$ is populated negligibly during the whole process (see Fig. 5.6c). A rather big difference to square pulses is the behaviour for increasing detuning. On contrary to square pulses, at certain values of detuning the population stays in the final state $|-1\rangle$ for the remaining pulse duration (see Fig. 5.6d), although the MW power is not yet zero.

Thinking about the wire grid a detuning of the transfer pulses has an additional advantage. Moving along one wire away from the site of the two-tone transfer, the signal power of the perpendicular wire decreases consequently and goes to zero as was mentioned before. Hence, starting at a certain distance a NV⁻ is only affected by the MW signal of the parallel wire and transitions happen in either the $|0\rangle \leftrightarrow |-1\rangle$ or the $|0\rangle \leftrightarrow |+1\rangle$ sub-system. From the perspective of the NV⁻ the wire grid is reduced to a single wire. Therefore, Rabi nutations of a single NV⁻ can be compared to two-tone measurements done with the chip at crossings farther away from the two-tone transfer site. Introducing a detuning, however, reduces the transfer probability depending on the MW power.

In Fig. 5.7a a MW signal with a power equal to a Rabi frequency of $2\pi \times 8.78$ MHz is applied and the time trace depending on the detuning is recorded. The duration of the MW pulse is in a range from 12.5 ns to 150 ns, while the detuning is scanned from 0 MHz to 40 MHz. In Fig. 5.7b the MW power is reduced to a value equal to a Rabi frequency of $2\pi \times 746$ kHz. As smaller MW power results in longer transfer-times, the pulse duration goes from 12.5 ns to 2000 ns. Vice versa, the detuning which is needed to stop a population transfer gets smaller. Therefore the detuning ranges from 0 MHz to 4 MHz. Fig. 5.7 shows that a detuning can be found for any applied MW power, at which a population transfer does not occur any more. A higher MW power requires a larger detuning.

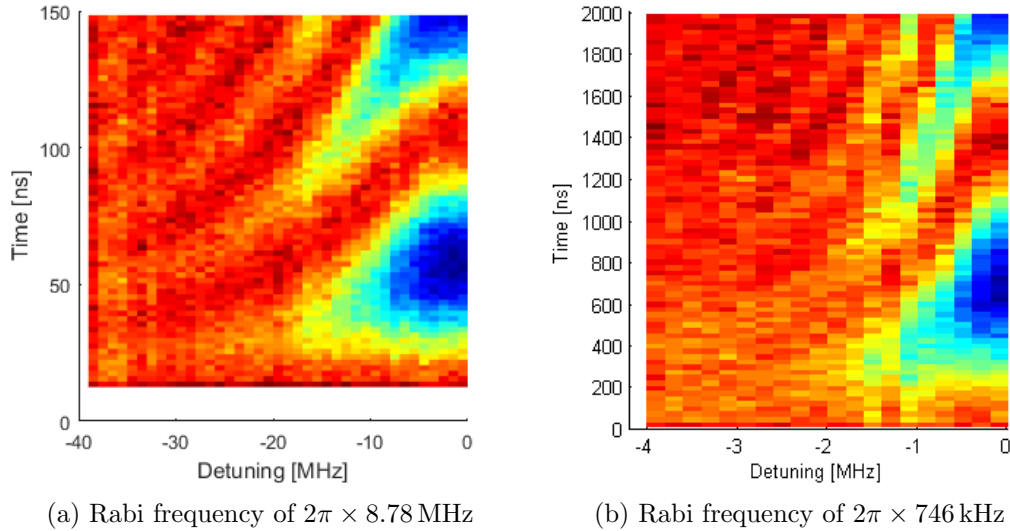


Fig. 5.7: Detuning scan of Rabi nutations. The NV^- is prepared in $|0\rangle$. The frequency of the applied MW signal is detuned by some amount and the time trace is observed. The color scale goes from blue (empty state) to red (occupied state). a.) The power of the resonant MW signal corresponds to a Rabi frequency of $2\pi \times 8.78$ MHz. b.) The power of the resonant MW signal corresponds to a Rabi frequency of $2\pi \times 746$ kHz.

To summarize the expectations of the performance of the wire grid chip:

- The transfer efficiency of the two-tone pulses decreases with increasing distance to the intended transfer-site (see fig. 5.4). Thus, a two-tone transfer at neighbouring junctions might not take place.
- However, sites along one of the two wires carrying the two-tone pulses might still perform partial population transfers in the $|0\rangle \leftrightarrow |+1\rangle$ ($|0\rangle \leftrightarrow |-1\rangle$) spin-sub-system. In order to oppress these transitions a detuning must be introduced (see Fig. 5.7).
- This detuning is needed as well for reducing the three-level spin-system to an effective $|-1\rangle \leftrightarrow |+1\rangle$ spin-system in order to avoid populating $|0\rangle$ during the two-tone transfer (see Fig. 5.5 and Fig. 5.6).

5.3 Chip

In the previous section the performance of the wire grid chip was anticipated by using qualitatively equal measurements done with single NV^- and a single wire. In the following section measurements done with the wire grid itself will be demonstrated, but first some thoughts have to be given to the change of the diamond sample from single NV^- to NV^- -ensemble.

In case of green laser initialization one has to consider, that ensembles consist of a huge amount of NV^- s and therefore a higher laser power is needed to make sure that as many

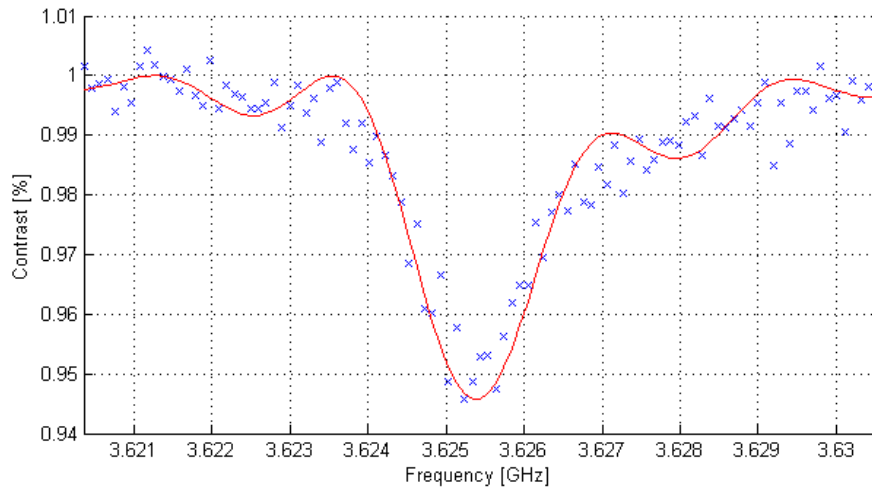


Fig. 5.8: ODMR of a NV⁻-ensemble with polarized nuclear spin. Scanning the MW frequency of an applied π -pulse with a power corresponding to a Rabi frequency of $2\pi \times 861$ kHz results in a spectrum with three resonance dips fitting the hyperfine transitions. The blue crosses are data points and the red curve is a fit function consisting of three functions according to Eq. 2.14 with a FWHM of ~ 1.39 MHz. A magnetic field of 27.0 mT is applied and by aligning the field vector with the NV⁻-axis a nuclear spin polarization of 84.0% is achieved.

NV⁻s as possible are initialized in $|0\rangle$. The thoughts about the efficiency are the same as for single NV⁻s, i.e. due to the transition probabilities in the optical cycles (see Fig. 2.2) a certain value of initialization efficiency cannot be exceeded.

Furthermore, in ensembles four orientations of the NV⁻-axis are possible. These different orientations have the effect that an arbitrary applied magnetic field is in general felt differently by each of the NV⁻-families as was already discussed in Sec. 4.1. The $|\pm 1\rangle$ energy states are shifted less or more for each family due to the Zeeman effect. If the magnetic field is aligned with the axis of one of the families, this family undergoes the largest energy shift, whereas the other three experience the same effective magnetic field. A MW π -pulse resonant with the most shifted NV⁻-family, therefore, transfers only one of the families from $|0\rangle$ to $|\pm 1\rangle$ while the others remain in $|0\rangle$. At least three fourths of the NV⁻s are always in the same state namely $|0\rangle$ and thus emit the same amount of photons per second for a specific laser power. This NV⁻-fluorescence can be seen as background. Only one fourth of the NV⁻s react to the MW pulse and contribute to the wanted signal. As a consequence the contrast of the obtained signal between the 'bright' and the 'dark' state is lower compared to single NV⁻-measurements.

The discussion of the transfer efficiency of MW π -pulses holds for NV⁻-ensembles as well as for single NV⁻. Either the π -pulse has to have high power in order to gain high transfer efficiencies - same order of magnitude as for single NV⁻ transitions. Or the magnetic field has to be increased and aligned to the NV⁻-axis of one of the NV⁻-families in order to polarize the nuclear spin. In Fig. 5.8 the magnetic field has a magnitude of 27.0 mT and the degree of nuclear spin polarization is $\sim 84.0\%$. Moreover, the contrast drop discussed

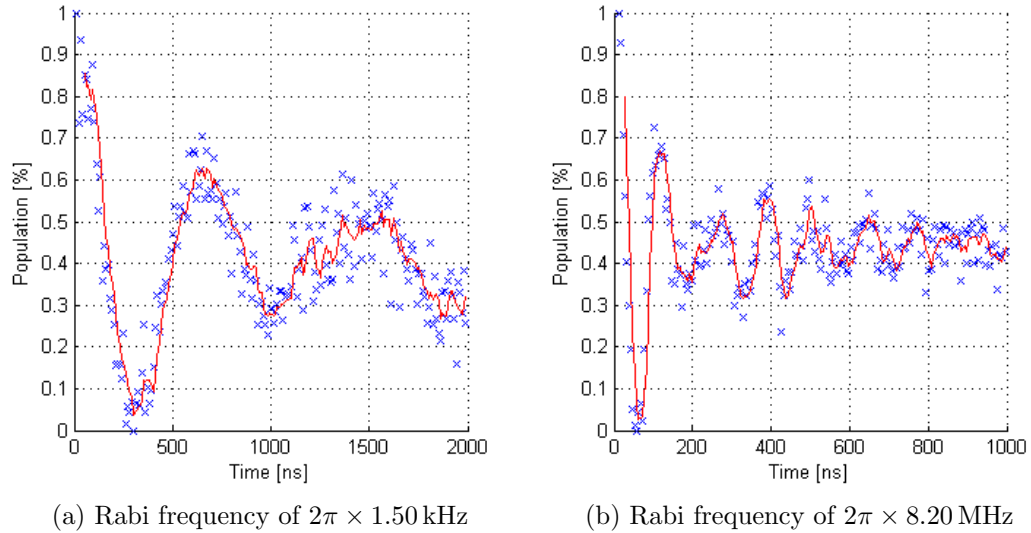


Fig. 5.9: Rabi nutation measurement performed with wire grid. Rabi oscillations are observed at different MW powers in order to show the interference of different Rabi frequencies mentioned in the text. The blue crosses are data points, while the red curve is a mean value over four data points. a.) The Rabi nutation with a frequency of $2\pi \times 1.5$ MHz is damped due to dephasing mechanisms. b.) The Rabi nutation with a main frequency of $2\pi \times 8.2$ MHz shows a collapse of the Rabi oscillation at ~ 200 ns due to destructive interference in the observed volume. At ~ 350 ns an oscillation is visible again, possibly due to partial re-phasing of the oscillations.

in the previous paragraph is seen clearly, if Fig. 5.8 is compared to single NV^- ODMR measurements from Fig. 5.3.

However, in contrary to single NV^- sequences MW pulses applied to ensemble samples cannot have an arbitrarily high power. In general a higher MW power results in faster Rabi oscillations, i.e. the Rabi frequency is increased. While a MW pulse applied to a single NV^- just increases the Rabi frequency with increasing power and has no effect on the decay envelope, NV^- ensembles show a collapse of the nutations after one or two periods at high MW powers (see Fig. 5.9). This can be explained by the fact that not a single NV^- is observed with the microscope but a whole volume of NV^- s. While the resolution in lateral direction is quite good (< 500 nm), the resolution in z-direction is worse (several μm) resulting in a certain observed volume. The magnetic field from the MW is not constant over the observed volume and thus results in many different Rabi frequencies. These Rabi oscillations can de-phase destructively and cause a collapse of the visibility. However, revivals are possible as well, if the Rabi oscillations interfere constructively before the dephasing mechanisms take over. Furthermore, a π -pulse, which transfers the NV^- s in a different state, is no true π -pulse for all NV^- s in the observed volume anymore, which causes worse transfer efficiencies. Thus, high MW powers (short π -pulses), which are wanted in case of single NV^- , are counter-productive for measurements

with NV⁻-ensembles. A physics-motivated lower limit of the MW pulse duration exists.

As has been already discussed in Sec. 5.2 the duration of the measurement sequence cannot be arbitrarily long either. The dephasing and decoherence time-constants T_1 , T_2 and T_2^* limit the duration of the measurement sequence. While the smallest time-constant, which is T_2^* , is still several tens of μs large in case of single NV⁻, the spin bath of all the NV⁻s in an ensemble reduce T_2^* drastically. T_2^* has a duration of $\sim 600\text{ ns}$ in the ensemble used for the wire grid measurements and is around two orders of magnitude smaller than for a single NV⁻. This reduction of the time-constant T_2^* as well as the discussed lower limit of the pulse duration due to too high MW power restrict the length of the transfer pulses between $\sim 50\text{ ns}$ and $\sim 1\ \mu\text{s}$.

Up to now only the change from a single NV⁻- to an ensemble-sample was discussed and more difficulties have arisen already:

- In order to initialize the ensemble in $|0\rangle$ as good as possible a higher green laser power is needed.
- Due to the additional NV⁻-families the contrast between 'bright' and 'dark' state is lower.
- The duration of the transfer pulses is limited on the one hand because of smaller dephasing and decoherence times and on the other hand due to differences in the Rabi frequencies in the observed volume for high MW powers.

Therefore good performance of the wire grid chip will be harder to handle than that of the single wire with a single NV⁻ of Sec. 5.2.

The behaviour of the wire grid was already anticipated in Sec. 5.2 and measurements on the wire grid itself will be done in the following paragraphs. The two-transfer in each measurement starts in $|+1\rangle$ and the π -pulses are determined for each set of measurements in order to guarantee the best initialization and read out. However, one has to keep in mind the worse performance due to the use of a NV⁻-ensemble as sample.

Firstly, in order to show that a two-tone pulse at a certain junction does hardly effect any other NV⁻s at other wire crossings the transfer efficiency depending on distance to the two-tone transfer site is determined. In order to compare these kind of measurements to the power sweep measurement done with single NV⁻ (see Fig. 5.4) the dependence of the MW power to the distance has to be determined. The magnetic field created by current I running in the y-direction along a wire of finite width w lying in the xy-plane is given by

$$\begin{aligned} B_x &= -\frac{\mu_0 I}{2\pi w} \left[\arctan\left(\frac{x+w/2}{y}\right) - \arctan\left(\frac{x-w/2}{y}\right) \right] \\ B_y &= \frac{\mu_0 I}{4\pi w} \log\left(\frac{(x+w/2)^2 + y^2}{(x-w/2)^2 + y^2}\right) \end{aligned} \quad (5.4)$$

where μ_0 is the vacuum permeability. The relative magnitude of this field $|B_{xz}|$ is shown in Fig. 5.10a.

The wires are very thin ($\sim 400\text{ nm}$) and have a width w of $10\ \mu\text{m}$, while the distance r to the transfer site is some tens of μm . Thus, the ratio $\frac{b}{r}$ is small and the wires can be assumed to be infinitely thin with respect to the distance to the transfer site. Fig.

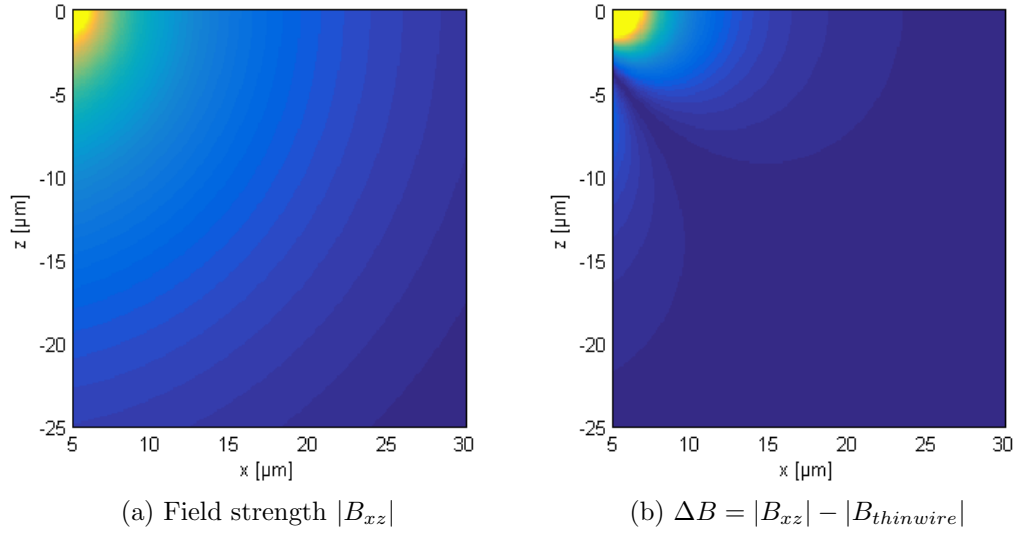


Fig. 5.10: Magnetic field of a thin but 10 μm broad wire. a.) The relative magnitude of the magnetic field is plotted over the distance to the centre of the wire (x) and over the depth (z). Most measurements are conducted at 10 μm distance to the wire-centre and in a depth of 15 μm. In this region the magnetic field vector is almost perpendicular to the NV-axis, which assures good transfer probability. While yellow depicts a large magnitude of the magnetic field and is set at 50 % of max $|B_{xz}|$, dark blue stands for low magnetic field magnitude. b.) The difference in magnitude of the magnetic fields of a broad wire and an ideal infinitely thin wire is plotted over the distance to the centre of the wire (x) and over the depth (z). At the site where most measurements are conducted ($x = 10$ μm, $z = 15$ μm) the difference is very small (about 0.1 % and thus the magnetic field is almost similar to Eq. 5.5. While yellow depicts a large difference of the magnetic field magnitude and is set at 25 % of max ΔB , dark blue stands for a small difference.

5.10b shows that the difference between real magnetic field and the magnetic field of an infinitely thin wire is very small at depths (z) larger than 15 μm and distances from the wire edge ($x - w$) larger than 5 μm, where the measurement is usually conducted. Thus the magnetic field strength of the MW pulses can be simply written as

$$B_{thinwire} = \frac{\mu_0 I}{2\pi r} \quad (5.5)$$

Finally, as the power of the MW is proportional to the square of the magnetic field ($p \propto |B|^2$) the power can be written in logarithmic scale with the help of Eq. 5.3 as

$$p(dBJ) = 10 \log_{10} \left(\frac{r_0^2}{r^2} \right) \quad (5.6)$$

where r_0 is the distance to the wire, where the two-tone transfer works best. A simple way to calculate the power from the distance to the wire edge has been found, with which

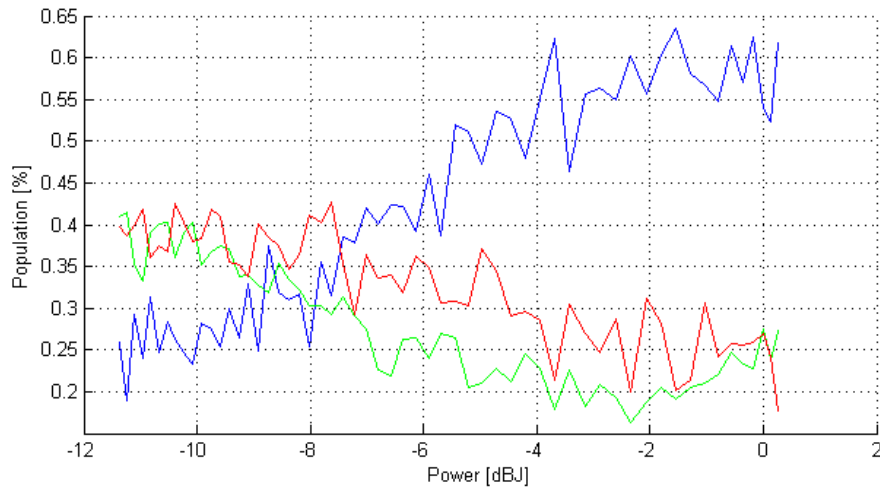


Fig. 5.11: Distance scan moving along one of the wires carrying the two-tone pulses performed with the wire grid. The NV⁻s are prepared in $|+1\rangle$ and a two-tone transfer is performed with a MW power corresponding to a Rabi frequency of $2\pi \times 2.10$ MHz and a detuning of 0 MHz. While the distance to the Ω_+ -wire is held constant, the distance to the Ω_- -wire is changed. The power is calculated according to Eq. 5.6. The red curve correspond to the population in $|+1\rangle$, the green one to $|0\rangle$ and the blue one to $|-1\rangle$.

the measurement done in Fig. 5.4 can be compared to the distance scan measurement performed with the wire grid (see Fig. 5.11).

The measurement is performed by changing the distance to the wire driving the Ω_- -pulses, while the distance to the Ω_+ -wire remains the same. Additionally the initialization and read-out pulses are all led through the Ω_+ -wire in order to assure efficient $|0\rangle \leftrightarrow |\pm 1\rangle$ transitions for all distances. The sequence starts as usual with the initialization in $|0\rangle$ via a green laser pulse - keep in mind that the laser power needs to be higher than in single NV⁻-measurements to have a high initialization efficiency. Afterwards the NV⁻ is transferred with a 100 ns π -pulse into state $|+1\rangle$. The MW power for the two-tone pulses are set at a certain distance r_0 in a way to get the best possible transfer efficiency. After choosing the parameters the distance is changed for each measurement and the dependence of the transfer efficiency is obtained. The state of the NV⁻ ($|\pm 1\rangle, |0\rangle$) after the two-tone pulses is read out by either applying a π -pulse resonant with $|0\rangle \leftrightarrow |\pm 1\rangle$ or applying no MW signal at all, respectively.

As expected, the overall performance of the ensemble sample is worse than that of the single NV⁻ sample. On the one hand the transfer efficiency is lower, as dephasing effects screw up a clean transfer. On the other hand more noise is measured due to the additional fluorescence of the other three NV⁻-families, which remain in $|0\rangle$. However, the dependence on the power from Fig. 5.11 is qualitatively similar. For smaller MW powers - larger distances to the wire - the efficiency of the two-tone transition decreases. The suggested behaviour anticipated with the power scan measurement from Fig. 5.4 is observed in the wire grid and the educated guess that the two-tone pulses hardly transfer

NV's from $|+1\rangle$ to $|-1\rangle$ at other crossings can be stuck to as well. Lastly, the importance of detuning of the two-tone pulses can be emphasized again. As the power of the Ω_- -pulse decreases the three-level ($|+1\rangle, |0\rangle, |-1\rangle$) system decreases to a two-level system ($|+1\rangle, |0\rangle$) and transitions between $|+1\rangle \Leftrightarrow |0\rangle$ still occur. By applying a detuning to the two-tone pulses these transitions can be avoided.

Finally, after showing that manipulating NV's only at a certain junction of the wire grid should be possible, the measurements themselves will follow in the next few paragraphs.

The measurement is done at four different junction of the wire grid: One at the actual site of the two-tone transfer (Figs. 5.12 a-c), one at each neighbour along the two wires driving the Ω_- - and Ω_+ pulses (Figs. 5.12 d-f and Figs. 5.13 a-c) and one at the nearest diagonal neighbour (Figs. 5.13 d-f). The measurements are done with the usual initialization and transfer sequence for two-tone transitions. On the one hand the state of the NV's is read out for changing durations of the two-tone pulses (y-axis), on the other hand the detuning of the two-tone pulses is changed after each duration scan (x-axis). The MW power of the two-tone pulses corresponds to a Rabi frequency of $2\pi \times 5.00$ MHz in the $|0\rangle \Leftrightarrow |\pm 1\rangle$ transitions and their shape is rectangular.

In Figs. 5.12 a-c the NV's are intended to do a transfer from $|+1\rangle$ to $|-1\rangle$. However, at small detunings $|0\rangle$ is populated. By increasing the detuning $|0\rangle$ gets less and less populated, while the transfer from $|+1\rangle$ to $|-1\rangle$ just needs more time to be completed. Meanwhile the efficiency of the two-tone transfer is only slightly decreased. A detuning can be found, where $|0\rangle$ does not get populated anymore but the efficiency is still reasonable. In case of Figs. 5.12 a-c this detuning would be around -12 MHz. The measurements at the site of the two-tone transfer are similar to those done with a single wire in Fig. 5.5. The wire grid fulfils the expectations regarding the two-tone transfer.

Moving along the Ω_+ -wire to the neighbouring junction reduces the effective power of the Ω_- -pulse at the observed site. In Figs. 5.12 d-f the occupation of each NV⁻ state is plotted again over detuning and pulse duration. While the population of $|-1\rangle$ stays the same for all measurements because of lack of MW power of the Ω_- -pulses, Rabi nutations between $|+1\rangle$ and $|0\rangle$ are observed. As anticipated in Sec. 5.2 the two-tone pulses get reduced to simple $|0\rangle \Leftrightarrow |+1\rangle$ transfer pulses. In good agreement with the detuned Rabi nutation measurements with a single NV⁻ from Fig. 5.7 the transfer efficiency between $|0\rangle$ and $|+1\rangle$ gets lower by increasing the detuning. Starting from a detuning of -12 MHz $|0\rangle$ hardly gets populated, which is a nice result as the detuning for the two-tone pulses at the site of the actual transfer should also be -12 MHz or more.

The measurements conducted when moving along the Ω_- -wire to the next junction are shown in Figs. 5.13 a-c. Therefore the power of the Ω_+ -pulse is decreased, similar as the Ω_- -signal before, and the two-tone pulses are reduced to $|0\rangle \Leftrightarrow |-1\rangle$ transfer pulses. However, as the NV's gets still initialized in $|+1\rangle$ before applying the two-tone pulses, the Ω_- -pulse has hardly any to no effect on the NV's and they remain in $|+1\rangle$ for all MW durations and detunings. Thus, NV's at all junctions but those along the Ω_+ -wire remain in $|+1\rangle$ even at zero detuning, if they have been initialized in $|+1\rangle$.

Lastly, the junction diagonal to the actual two-tone transfer site gets looked at (Figs. 5.13 d-f). At this junction the power of the Ω_+ - as well as the Ω_- -pulse is small and as expected the NV's do barely respond to the two-tone pulses at all.

After describing the effects of the two-tone pulses at the individual crossings a chosen

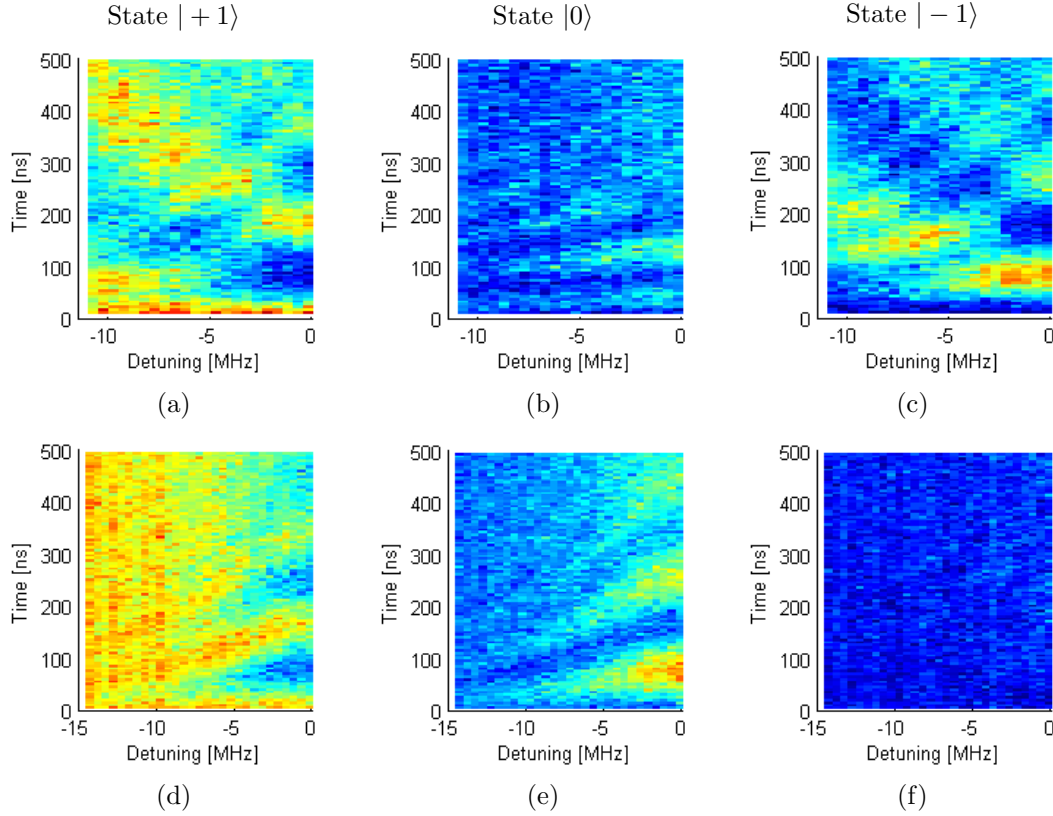


Fig. 5.12: Detuning scan of rectangular two-tone pulses performed with the wire grid at different crossings. The NV⁻s are prepared in $|+1\rangle$. The MW of the two-tone pulses corresponds to a Rabi frequency of $2\pi \times 5.00$ MHz. The color scale goes from blue (empty state) to red (occupied state). a.)-c.) Detuning scan at actual transfer site. d.)-f.) Detuning scan at neighbour along Ω_+ -wire

detuning and time point at which the two-tone transfer shows promising success while the effects at other crossings are rather small is discussed. The chosen point is at a detuning of -6 MHz and a MW duration of 150 ns. The population probability for the individual states at different crossings is plotted in Fig. 5.14 after the two-tone transfer is completed.

At the crossing along the Ω_+ -wire (blue) the largest part of the NV⁻s remain in the initial state $|+1\rangle$ (59%). State $|0\rangle$ is populated with a probability of 27% and $|-1\rangle$ with a probability of 14%. The power of the Ω_- -pulse is close to zero due to the large distance to the Ω_- -wire and thus, the two-tone transfer pulses are reduced to $|0\rangle \leftrightarrow |+1\rangle$ -transition pulses. Rabi oscillations between $|0\rangle \leftrightarrow |+1\rangle$ occur and as the detuning is not yet big enough a small part of the NV⁻s are still transferred explaining the population probability of 27% of state $|0\rangle$.

At the crossing along the Ω_- -wire (azure) most of the NV⁻s stay in the initial state $|+1\rangle$ (76%). The power of the Ω_+ -pulse is almost zero meaning that the two-tone pulses are reduced to $|0\rangle \leftrightarrow |-1\rangle$ -transition pulses. The NV⁻s, however, are initialized in $|+1\rangle$ and thus the two-tone pulses have hardly any effect on the NV⁻s resulting in the high

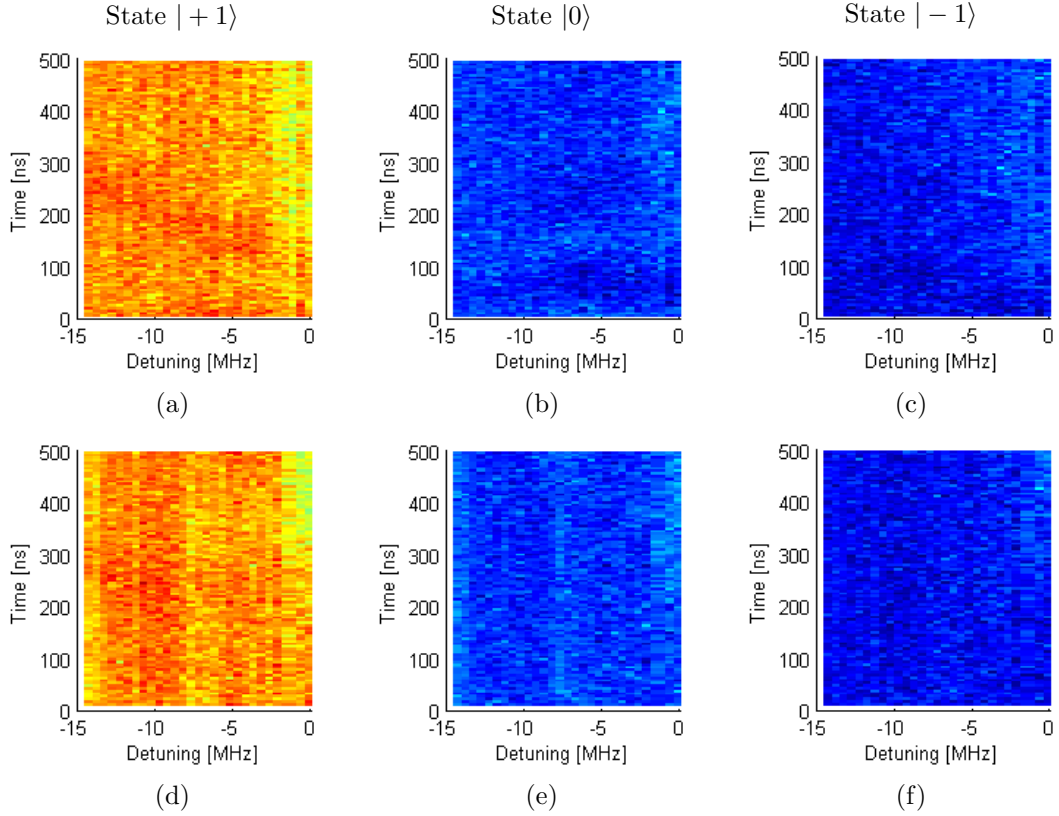


Fig. 5.13: Detuning scan of rectangular two-tone pulses performed with the wire grid at different crossings. The NV-s are prepared in $|+1\rangle$. The MW of the two-tone pulses corresponds to a Rabi frequency of $2\pi \times 5.00$ MHz. The color scale goes from blue (empty state) to red (occupied state). a.)-c.) Detuning scan at neighbour along Ω_- -wire. d.)-f.) Detuning scan at diagonal neighbour.

population probability of $|+1\rangle$. The remaining population probability of the other two states ($|0\rangle \rightarrow 19\%$ and $|-1\rangle \rightarrow 5\%$) can be explained by the already discussed imperfect laser light initialization and the non-perfect MW- π -pulses.

The NV-s at the crossing diagonal to the intended two-tone transfer site (yellow) are least affected by the two-tone pulses as the Ω_+/Ω_- -wires are quite distant, i.e. the power of the two-tone pulses are very small. The NV-s remain in the initial state $|+1\rangle$ (76%) and as before the population probability of $|0\rangle$ (17%) and $|-1\rangle$ (7%) can be explained by the imperfect laser light initialization and the non-perfect MW- π -pulses.

The NV-s at the crossing where the two-tone transition is intended (red) are transferred with a high success rate from $|+1\rangle$ to $|-1\rangle$, while the population probability of $|0\rangle$ is within the expected values due to imperfections in initialization. The efficiency of two-tone transfer remains nearly the same when implementing a detuning on the two-tone pulses, because the transfer occurs via a 'virtual' state. As a result, the NV-s in state $|0\rangle$ remain nearly unaffected by the two-tone pulses during the whole transfer (12%). The initial state $|+1\rangle$ remains populated with a probability of 23%, while $|-1\rangle$ has a population

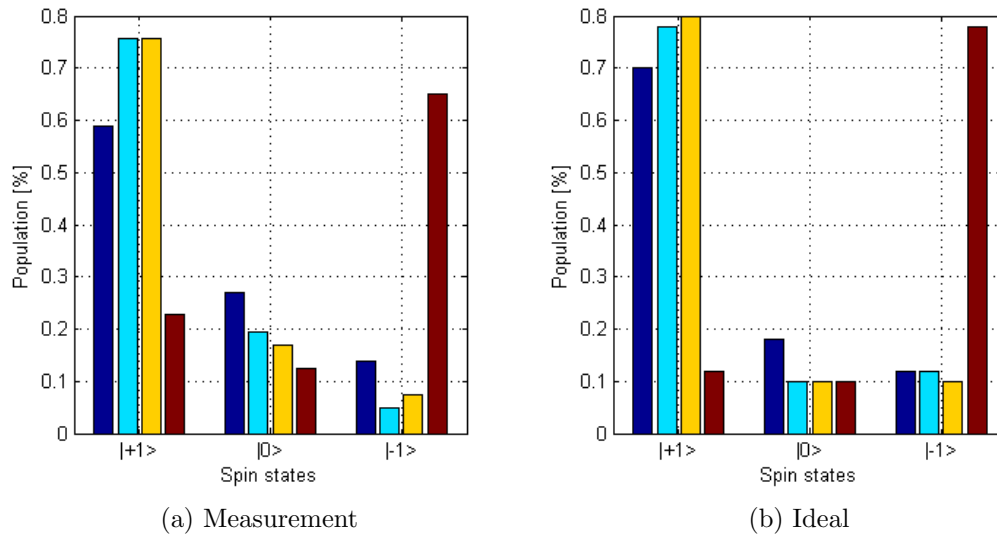


Fig. 5.14: Population probability for the individual states at different crossings. A detuning of -6 MHz and a MW duration of 150 ns are chosen to demonstrate the effects of the two-tone pulses. a.)+b.) Blue depicts the neighbouring junction along the Ω_- -wire, while azure represents the neighbouring junction along the Ω_+ -wire. The crossing diagonal to the intended two-tone transfer site is depicted by yellow and the site of the actual two-tone transfer is shown in red. The population probability after a two-tone transfer sequence is plotted over the three different spin states of the NV $^-$ ($|+1\rangle$, $|0\rangle$ and $|-1\rangle$). a.) The population probability from the measurements performed in Figs. 5.12 and 5.13 is plotted. b.) The population probability for the ideal case of no dephasing but imperfect initialization ($| - 1 \rangle \rightarrow 10\%$, $|0\rangle \rightarrow 10\%$, $|+1\rangle \rightarrow 80\%$) is plotted.

probability of 65% after the two-tone transfer. A successful two-tone transfer of most NV $^-$ s has been accomplished.

In summary the two-tone transition at the intended site is performed with a good transfer efficiency, while the effects at other crossings are kept within a limit. Overall, the NV $^-$ s at the intended crossing are in state $| - 1 \rangle$ while the NV $^-$ s at all other junctions remain in $| + 1 \rangle$. A grid of NV $^-$ s in state $| + 1 \rangle$ but a single site is accomplished. Hence, addressing a single qubit within a large number of qubits is achieved with the wire grid proposed in this thesis.

Theoretically using \sin^2 -pulses instead of rectangular ones should have a better performance as the condition of adiabatic following mentioned in Sec. 2.6 is mostly fulfilled. However, \sin^2 -pulses need a longer time to finish the two-tone transfer. Unfortunately, the duration of the two-tone transition is limited by the dephasing time of the NV $^-$ -ensemble and T_2^* is too small (~ 600 ns) to perform two-tone transitions with \sin^2 -pulses.

After showing that the wire grid can be used to transfer NV $^-$ s at a single site from one state to another with hardly affecting the NV $^-$ s at other sites a way to cancel out a MW signal totally at the neighbouring wire is demonstrated. The idea is to run a counteracting

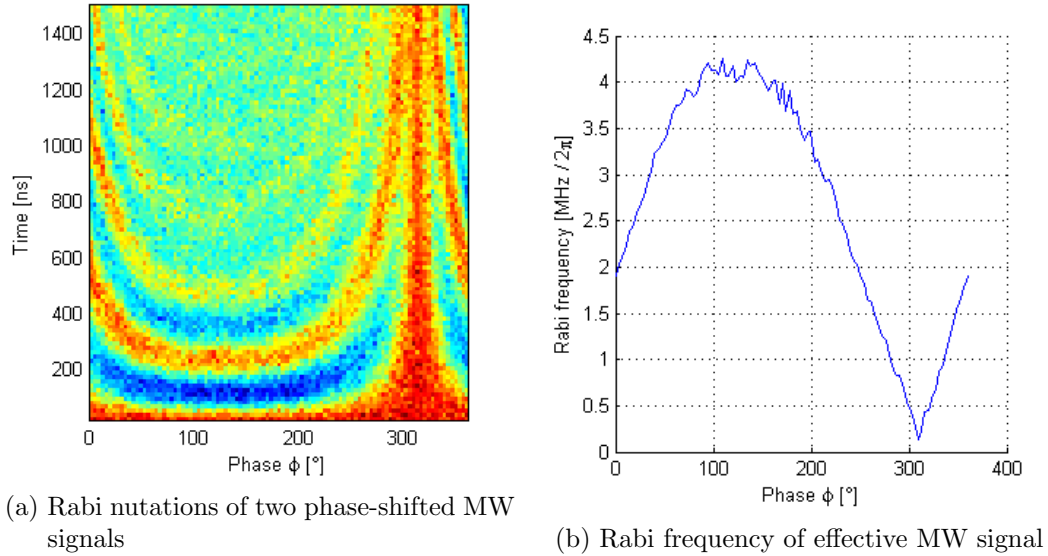


Fig. 5.15: Rabi nutations depending on the phase difference between two MW signals. By applying two phase-correlated MW signals on neighbouring wires and changing the phase constructive and destructive classical interference of the MW signals can be observed. The measurement was conducted about $10\ \mu\text{m}$ from the wire edge and with a MW power of each signal equal to a Rabi frequency of $2\pi \times 2.17\text{MHz}$. a.) Rabi oscillations are observed depending on the phase between the MW signals. The colors represent an occupied state $|0\rangle$ (red) and an empty state $|0\rangle$ (blue). b.) The Rabi frequency depending on the phase is calculated from each time-trace by using a cosine fit function with an exponential decay envelope.

signal through the neighbouring wire to cancel out the MW signal from the pulse sequence. In order to do so the two signals have to have a phase correlation and the phase of at least one of the signals has to be tunable. In theory, every MW pulse regardless of its shape should be cancellable. However, the principle is demonstrated with simple rectangular pulses and Rabi nutation-like measurements.

Both MW signals come from the same MW source (Anritsu 3691B) and are split using a power-splitter to guarantee a phase correlation. Afterwards one is led via a switch and an amplifier directly to the experiment. The other is fed through an IQ-mixer first as the IQ-mixer has the property to tune the phase ϕ of the signal [23]

$$\tan \phi(t) = \frac{Q(t)}{I(t)} \quad (5.7)$$

where $I(t)$ and $Q(t)$ are the two input signals of the IQ-mixer. As only rectangular pulses are applied the two input signals are constant in time: $I(t) = I$ and $Q(t) = Q$. By choosing the ratio between I and Q the phase ϕ of the MW signal is set. However, I and Q can not be chosen completely freely, because the effective amplitude $A = \sqrt{I^2 + Q^2}$ has to have the same value for all phases.

The measurement is conducted close to one of the two wires (distance to wire edge $\sim 10\ \mu\text{m}$) and with a MW power of each signal equal to a Rabi frequency of $2\pi \times 2.17\ \text{MHz}$. The ratio between I and Q is changed, while the effective MW power remains constant. The Rabi nutations depending on the phase are recorded, which is pictured in Fig. 5.15a, and the Rabi frequency is determined and plotted in Fig. 5.15b. The maximal Rabi frequency is observed at $\phi = 127.3^\circ$ and has an value of roughly double the individual Rabi frequencies ($2\pi \times (2 \times 2.17\ \text{MHz}) \sim 2\pi \times 4.25\ \text{MHz}$). An expected result as the two MW signal simply add up and produce an effective magnetic field of double the magnitude of the individual MW pulses. Moreover, a phase can be found, where the Rabi nutations nearly disappear, i.e. the Rabi frequency is close to zero, at $\phi = 309.1^\circ$. The difference between maximal and minimal Rabi frequency is about 180° , which agrees nicely with the phase shift between two cosine functions.

It has been demonstrated that cancelling out a MW signal at a chosen site using a second phase-correlated MW pulse is possible. The implementation of this knowledge in the two-tone sequence, however, would go beyond the scope of this thesis.

6 Conclusion and Outlook

The work of this thesis has demonstrated a fairly simple way to create a scalable qubit system. The spin states ($m_s = \pm 1$) of a NV^- serve as qubit and microwaves are used as initializing, read-out and transfer mechanism.

After introducing the principle of two-tone transfer the anticipated performance of the wire grid is demonstrated using a single NV^- sample and a single gold wire (Sec. 5.2). From these measurements can be concluded that a single site at a certain crossing of the wire can be addressed without transferring NV^- s at other junctions by introducing a detuning. The measurements with the wire grid (Sec. 5.3) confirm the anticipated statements. For increasing distance to the two-tone transfer site the efficiency of the two-tone transition decreases. At the neighbouring junction the two-tone transfer probability is close to zero, even with a MW power equal to a Rabi frequency of $2\pi \times 5.00$ MHz. While the efficiency of the two-tone transfer is hardly affected by the detuning, transitions at other crossings, especially those along the wires driving the two-tone pulses, hardly occur starting from a certain detuning. If there should be still some MW signal at the neighbouring wire, a counteracting pulse can cancel out any transitions.

Using the wire grid and detuned MW signals a single site can be manipulated, while all other sites are unaffected. Therefore, a single qubit can be changed within a system of qubits. Furthermore, the number of sites of wire grid scales quadratically with the number of wire pairs and thus a large system of qubits can be achieved easily.

However, there is still much room for improvements concerning the wire grid. A quite obvious improvement is switching from NV^- -ensemble sample to a single NV^- diamond. As demonstrated in Sec. 5.2 the single NV^- sample has on the one hand much longer dephasing and decoherence time constants and thus more complex MW pulses can be driven in order to transfer the NV^- adiabatically. On the other hand the contrast between the different spin states of NV^- is much higher resulting in better distinguishability and higher fidelity of the population probability of the spin states. However, producing diamond samples with single NV^- s only at chosen sites is difficult. Furthermore, the alignment of the single NV^- s with the wire grid is a hard task, but the benefits of using single NV^- s would be worth the effort. Another improvement can be achieved by implementing the cancelling MW signal in the sequence and avoid unintended transitions. The next step will be to address several sites successively and increase the efficiency of the two-tone transition.

To conclude, in this work I have demonstrated that qubit arrays can be addressed in a scalable manner using two-tone addressing in a wire grid system. This result is not unique to NV^- centres, but can potentially be used for any system with a spin greater than $\frac{1}{2}$. Finally, I showed that classical interference can be used to remove any remaining cross-talk between neighbouring sites. Taken together, these results demonstrate that the addressing method is promising for numerous applications, including quantum sensor arrays and quantum information processing.

Bibliography

- [1] T. D. Ladd et al. “Quantum computers”. In: *Nature* 464.7285 (2010), pp. 45–53. ISSN: 0028-0836. DOI: 10.1038/nature08812 (cit. on pp. 1, 3, 4).
- [2] Rainer Blatt and David Wineland. “Entangled states of trapped atomic ions”. In: *Nature* 453.7198 (2008), pp. 1008–1015. ISSN: 0028-0836. DOI: 10.1038/nature07125 (cit. on pp. 1, 2).
- [3] K. R. Brown, Kim J., and C. Monroe. “Co-Designing a Scalable Quantum Computer with Trapped Atomic Ions”. In: *arXiv:1602.02840* (2016) (cit. on p. 1).
- [4] B. Lekitsch et al. “Blueprint for a microwave trapped-ion quantum computer”. In: *arXiv:1508.00420* (2015) (cit. on p. 1).
- [5] Immanuel Bloch. “Quantum coherence and entanglement with ultracold atoms in optical lattices”. In: *Nature* 453.7198 (2008), pp. 1016–1022. ISSN: 0028-0836. DOI: 10.1038/nature07126 (cit. on pp. 1, 2).
- [6] Yang Wang et al. “Single-qubit gates based on targeted phase shifts in a 3D neutral atom array”. In: *Science (New York, N.Y.)* 352.6293 (2016), pp. 1562–1565. ISSN: 0036-8075. DOI: 10.1126/science.aaf2581 (cit. on pp. 1, 2).
- [7] M. Saffman, T. G. Walker, and K. Mølmer. “Quantum information with Rydberg atoms”. In: *Reviews of Modern Physics* 82.3 (2010), pp. 2313–2363. ISSN: 0034-6861. DOI: 10.1103/RevModPhys.82.2313 (cit. on pp. 1, 3, 4).
- [8] John Clarke and Frank K. Wilhelm. “Superconducting quantum bits”. In: *Nature* 453.7198 (2008), pp. 1031–1042. ISSN: 0028-0836. DOI: 10.1038/nature07128 (cit. on pp. 1, 3, 4).
- [9] Pieter Kok et al. “Linear optical quantum computing with photonic qubits”. In: *Reviews of Modern Physics* 79.1 (2007), pp. 135–174. ISSN: 0034-6861. DOI: 10.1103/RevModPhys.79.135 (cit. on p. 1).
- [10] W. B. Gao et al. “Coherent manipulation, measurement and entanglement of individual solid-state spins using optical fields”. In: *Nature Photonics* 9.6 (2015), pp. 363–373. ISSN: 1749-4885. DOI: 10.1038/NPHOTON.2015.58 (cit. on pp. 1, 4).
- [11] Marcus W. Doherty et al. “The nitrogen-vacancy colour centre in diamond”. In: *Physics Reports* 528.1 (2013), pp. 1–45. ISSN: 03701573. DOI: 10.1016/j.physrep.2013.02.001 (cit. on pp. 1, 5, 13, 15, 42).
- [12] G. Davies. “The A nitrogen aggregate in diamond-its symmetry and possible structure”. In: *Journal of Physics C: Solid State Physics* 9.19 (1976), pp. L537–L542. ISSN: 0022-3719. DOI: 10.1088/0022-3719/9/19/005 (cit. on p. 9).

-
- [13] F. Jelezko and J. Wrachtrup. “Single defect centres in diamond: A review”. In: *physica status solidi (a)* 203.13 (2006), pp. 3207–3225. ISSN: 18626300. DOI: 10.1002/pssa.200671403 (cit. on p. 10).
- [14] J. O. Orwa et al. “An upper limit on the lateral vacancy diffusion length in diamond”. In: *Diamond and Related Materials* 24 (2012), pp. 6–10. ISSN: 09259635. DOI: 10.1016/j.diamond.2012.02.009 (cit. on p. 9).
- [15] V. M. Acosta et al. “Diamonds with a high density of nitrogen-vacancy centers for magnetometry applications”. In: *Physical Review B* 80.11 (2009). ISSN: 1098-0121. DOI: 10.1103/PhysRevB.80.115202 (cit. on p. 9).
- [16] Tobias Nöbauer et al. “Creation of ensembles of nitrogen-vacancy centers in diamond by neutron and electron irradiation”. In: (2013). URL: <https://arxiv.org/abs/1309.0453> (cit. on p. 9).
- [17] M. W. Doherty et al. “The negatively charged nitrogen-vacancy centre in diamond: The electronic solution”. In: *New Journal of Physics* 13.2 (2011), p. 025019. ISSN: 1367-2630. DOI: 10.1088/1367-2630/13/2/025019 (cit. on p. 10).
- [18] R. P. Messmer and G. D. Watkins. “Linear Combination of Atomic Orbital-Molecular Orbital Treatment of the Deep Defect Level in a Semiconductor: Nitrogen in Diamond”. In: *Physical Review Letters* 25.10 (1970), pp. 656–659. ISSN: 0031-9007. DOI: 10.1103/PhysRevLett.25.656 (cit. on p. 10).
- [19] L. J. Rogers et al. “Time-averaging within the excited state of the nitrogen-vacancy centre in diamond”. In: *New Journal of Physics* 11.6 (2009), p. 063007. ISSN: 1367-2630. DOI: 10.1088/1367-2630/11/6/063007 (cit. on p. 10).
- [20] V. M. Acosta et al. “Optical properties of the nitrogen-vacancy singlet levels in diamond”. In: *Physical Review B* 82.20 (2010). ISSN: 1098-0121. DOI: 10.1103/PhysRevB.82.201202 (cit. on p. 11).
- [21] M. Steiner et al. “Universal enhancement of the optical readout fidelity of single electron spins at nitrogen-vacancy centers in diamond”. In: *Physical Review B* 81.3 (2010). ISSN: 1098-0121. DOI: 10.1103/PhysRevB.81.035205 (cit. on p. 11).
- [22] N. Aslam et al. “Photo-induced ionization dynamics of the nitrogen vacancy defect in diamond investigated by single-shot charge state detection”. In: *New Journal of Physics* 15.1 (2013), p. 013064. ISSN: 1367-2630. DOI: 10.1088/1367-2630/15/1/013064 (cit. on p. 12).
- [23] Andreas Angerer. “Robust coherent optimal control of nitrogen-vacancy quantum bits in diamond”. Diploma thesis. Vienna: Technical University Vienna, 2013 (cit. on pp. 13, 17, 18, 58).
- [24] Gopalakrishnan Balasubramanian et al. “Ultralong spin coherence time in isotopically engineered diamond”. In: *Nature materials* 8.5 (2009), pp. 383–387. ISSN: 1476-1122. DOI: 10.1038/nmat2420 (cit. on p. 14).
- [25] Benjamin Smeltzer, Lilian Childress, and Adam Gali. “ ^{13}C hyperfine interactions in the nitrogen-vacancy centre in diamond”. In: *New Journal of Physics* 13.2 (2011), p. 025021. ISSN: 1367-2630. DOI: 10.1088/1367-2630/13/2/025021 (cit. on pp. 15, 16).

-
- [26] J. H. N. Loubser and J. A. van Wyk. “Electron spin resonance in the study of diamond”. In: *Reports on Progress in Physics* 41.8 (1978), pp. 1201–1248. ISSN: 0034-4885. DOI: 10.1088/0034-4885/41/8/002 (cit. on p. 16).
- [27] Mark Fox. *Quantum Optics: An Introduction (Oxford master series in physics ; 6)*. Oxford University Press, 2006 (cit. on pp. 16–19).
- [28] K. Bergmann, H. Theuer, and B. W. Shore. “Coherent population transfer among quantum states of atoms and molecules”. In: *Reviews of Modern Physics* 70.3 (1998), pp. 1003–1025. ISSN: 0034-6861. DOI: 10.1103/RevModPhys.70.1003 (cit. on pp. 21, 24).
- [29] V. I. Romanenko and L. P. Yatsenko. “Adiabatic population transfer in the three-level Lambda-system: Two-photon lineshape”. In: *Optics Communications* 140.4-6 (1997), pp. 231–236. ISSN: 00304018. DOI: 10.1016/S0030-4018(97)00152-1 (cit. on p. 21).
- [30] J. R. Kuklinski et al. “Adiabatic population transfer in a three-level system driven by delayed laser pulses”. In: *Physical Review A* 40.11 (1989), pp. 6741–6744. ISSN: 0556-2791. DOI: 10.1103/PhysRevA.40.6741 (cit. on p. 24).
- [31] T. Nöbauer. “Sensing, coherent coupling and optimal control with nitrogen-vacancy colour centres in diamond”. PhD Thesis. Vienna: Technical University Vienna, 2013 (cit. on p. 25).
- [32] Ran Fischer et al. “Optical polarization of nuclear ensembles in diamond”. In: *Physical Review B* 87.12 (2013). ISSN: 1098-0121. DOI: 10.1103/PhysRevB.87.125207 (cit. on pp. 26, 29, 32, 43).
- [33] V. Jacques et al. “Dynamic polarization of single nuclear spins by optical pumping of nitrogen-vacancy color centers in diamond at room temperature”. In: *Physical review letters* 102.5 (2009), p. 057403. ISSN: 0031-9007. DOI: 10.1103/PhysRevLett.102.057403 (cit. on p. 43).

List of Figures

1.1	Trapped, laser-cooled atomic ions and ultracold, neutral atoms in an optical lattice	2
1.2	Rydberg atoms and superconducting qubits	4
1.3	Wire grid scheme and three-level energy scheme of the NV ⁻ ground spin state	6
2.1	Structure of the NV	10
2.2	Term scheme of NV	11
2.3	Emission spectra of a single NV	12
2.4	Fluorescence time trace of NV ⁻	13
2.5	Fine- and hyperfine structure of NV ⁻ coupled to spin- $\frac{1}{2}$ nucleus	14
2.6	Fine- and hyperfine structure of NV ⁻ coupled to ¹⁴ N	15
2.7	Two-level approximation	17
2.8	Two-level transition	18
2.9	Inverse Λ -scheme of the NV ⁻ spin-1 ground state	21
2.10	Stimulated Raman adiabatic passage	23
3.1	Sketch of the optical setup	26
3.2	Sketch of the microwave chain	27
4.1	Optically detected magnetic resonance measurement	30
4.2	Rabi nutation measurement	31
4.3	Free induction decay measurement	33
4.4	Spin echo measurement	34
4.5	Two-tone transition measurement	36
4.6	Required MW transitions in order to perform two-tone transfer	37
5.1	Wire grid chip mounted on a PCB board	40
5.2	Production steps of wire grid chip	41
5.3	ODMR of a single NV ⁻ with polarized nuclear spin	44
5.4	Power scan of one of the two-tone pulses performed with a single NV ⁻	45
5.5	Detuning scan of rectangular two-tone pulses performed with a single NV ⁻	46
5.6	Detuning scan of \sin^2 two-tone pulses performed with a single NV ⁻	47
5.7	Detuning scan of Rabi nutations	48
5.8	ODMR of a NV ⁻ -ensemble with polarized nuclear spin	49
5.9	Rabi nutation measurement performed with wire grid	50
5.10	Magnetic field of a thin but 10 μm broad wire	52
5.11	Distance scan moving along one of the wires carrying the two-tone pulses performed with the wire grid	53

5.12	Detuning scan of rectangular two-tone pulses performed with the wire grid at different crossings (1/2)	55
5.13	Detuning scan of rectangular two-tone pulses performed with the wire grid at different crossings (2/2)	56
5.14	Population probability for the individual states at different crossings	57
5.15	Rabi nutations depending on the phase difference between two MW signals	58